

COORDINATED X-RAY, ULTRAVIOLET, OPTICAL, AND RADIO OBSERVATIONS OF THE PSR J1023+0038 SYSTEM IN A LOW-MASS X-RAY BINARY STATE

SLAVKO BOGDANOV¹, ANNE M. ARCHIBALD², CEES BASSA², ADAM T. DELLER², JULES P. HALPERN¹, GEORGE HEALD^{2,3},
 JASON W. T. HESSELS^{2,4}, GEMMA H. JANSSEN², ANDREW G. LYNE⁵, JAVIER MOLDÓN², ZSOLT PARAGI⁶,
 ALESSANDRO PATRUNO^{7,2}, BENETGE B. P. PERERA⁵, BEN W. STAPPERS⁵, SHRIHARSH P. TENDULKAR⁸,
 CAROLINE R. D'ANGELO⁷, RUDY WIJNANDS⁴

Submitted to the Astrophysical Journal on December 16, 2014

ABSTRACT

The PSR J1023+0038 binary system hosts a neutron star and a low-mass, main-sequence-like star. It switches on year timescales between states as an eclipsing radio millisecond pulsar and a low-mass X-ray binary. We present a multi-wavelength observational campaign of PSR J1023+0038 in its most recent low-mass X-ray binary state. Two long *XMM-Newton* observations reveal that the system spends $\sim 70\%$ of the time in a $\sim 3 \times 10^{33} \text{ erg s}^{-1}$ X-ray luminosity mode, which, as shown in Archibald et al. (2014), exhibits coherent X-ray pulsations. This emission is interspersed with frequent lower flux mode intervals with $\sim 5 \times 10^{32} \text{ erg s}^{-1}$ and sporadic flares reaching up to $\sim 10^{34} \text{ erg s}^{-1}$, with neither mode showing significant X-ray pulsations. The switches between the three flux modes occur on timescales of order 10 s. In the UV and optical, we observe occasional intense flares coincident with those observed in X-rays. Our radio timing observations reveal no pulsations at the pulsar period during any of the three X-ray modes, presumably due to complete quenching of the radio emission mechanism by the accretion flow. Radio imaging detects highly variable, flat-spectrum continuum emission from PSR J1023+0038, which likely originates in a weak jet-like outflow. Our concurrent X-ray and radio continuum data sets do not exhibit any correlated behavior. The observational evidence we present bears qualitative resemblance to the behavior predicted by some existing propeller and trapped disk accretion models although none can fully account for all aspects of the rich phenomenology of this system.

Subject headings: pulsars: general — pulsars: individual (PSR J1023+0038) — stars: neutron — X-rays: binaries

1. INTRODUCTION

PSR J1023+0038 (also known as AY Sextantis or FIRST J102347.6+003841) is a 1.7 ms pulsar in a 4.75 hour binary orbit around a bloated $\sim 0.2 M_{\odot}$ main-sequence-like companion star. This system is notable in that it was the first to exhibit compelling evidence for the transition process between an accretion disk-dominated low-mass X-ray binary-like state and a disk-free radio pulsar state. Optical observations revealed an accretion disk in the system in 2001 (Bond et al. 2002; Szkody et al. 2003; Wang et al. 2009), which appeared to be absent in early 2003 (Thornstensen & Armstrong 2005) and at the time of the radio pulsar discovery

(Archibald et al. 2009). During its disk episode in 2001, the binary appeared optically blue and bright in addition to showing strong, double-peaked H and He emission lines, which are commonly seen in low-mass X-ray binaries (LMXBs), and are a typical feature of accretion disks. This suggests that the companion star overflowed its Roche lobe, forming a disk surrounding the millisecond pulsar (MSP). In contrast, spectra obtained starting in early 2003 showed a substantially lower optical flux and a typical G-type spectrum, implying the absence of a substantial accretion disk.

A recent torrent of developments have revealed two close analogs to PSR J1023+0038. In 2013 March, PSR J1824–2452I in the globular cluster M28 was seen to switch between rotation-powered (radio) and high-luminosity accretion-powered (X-ray) pulsations (Papitto et al. 2013), thereby strengthening the long-suspected evolutionary link between LMXBs and “recycled” pulsars (Alpar et al. 1982). In addition, re-examination of archival optical and X-ray data of the X-ray binary XSS J12270–4859 revealed that only a few months prior (in 2012 November/December) its accretion disk had disappeared and the 1.7-ms radio pulsar became active (Bassa et al. 2014; Bogdanov et al. 2014b; Roy et al. 2014). See Linares (2014) for an overview of the X-ray states of these and analogous objects.

Unexpectedly, on 2013 June 23, no radio pulsations were detected from PSR J1023+0038, and none have been detected up to the submission of this manuscript

¹ Columbia Astrophysics Laboratory, Columbia University, 550 West 120th Street, New York, NY 10027, USA; slavko@astro.columbia.edu

² ASTRON, the Netherlands Institute for Radio Astronomy, Postbus 2, 7990 AA, Dwingeloo, The Netherlands

³ Kapteyn Astronomical Institute, University of Groningen, PO Box 800, 9700 AV, Groningen, The Netherlands

⁴ Anton Pannekoek Institute for Astronomy, University of Amsterdam, Science Park 904, 1098 XH Amsterdam, The Netherlands

⁵ Jodrell Bank Centre for Astrophysics, School of Physics and Astronomy, The University of Manchester, Manchester M13 9PL, UK

⁶ JIVE, Joint Institute for VLBI in Europe, Postbus 2, 7990 AA Dwingeloo, The Netherlands

⁷ Leiden Observatory, Leiden University, PO Box 9513, 2300 RA, Leiden, The Netherlands

⁸ California Institute of Technology, 1200 East California Boulevard, Pasadena, CA 91125, USA

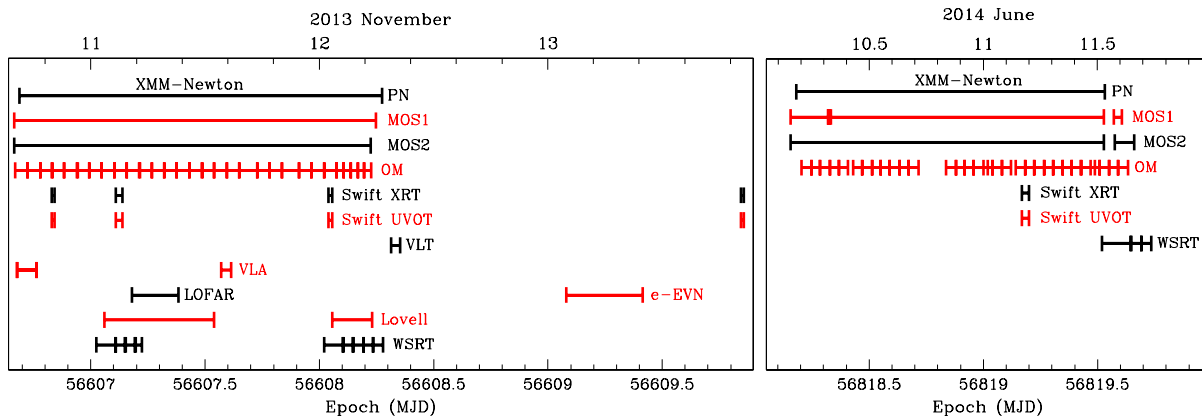


FIG. 1.— Timeline of the contemporaneous or near-contemporaneous multi-wavelength observations presented in this paper. The color variation is provided for ease of interpretation.

despite an intensified monitoring campaign and higher-radio-frequency observations with greater sensitivity. Subsequent X-ray, optical, and γ -ray investigation revealed that PSR J1023+0038 has undergone another transformation to an accretion disk-dominated state (Patruno et al. 2014; Stappers et al. 2014; Halpern et al. 2013; Tendulkar et al. 2014). This transition was accompanied by an extraordinary five-fold increase in γ -ray luminosity (Stappers et al. 2014). The X-ray emission observed by *Swift* XRT revealed a significant change in behavior compared to the disk-free state as well: in addition to an increase in flux by over an order of magnitude to $\sim 10^{33-34}$ erg s $^{-1}$, the orbital-phase-dependent modulations had disappeared, replaced by aperiodic variability with rapid drops to a low flux level. Follow-up hard X-ray observations with *NuSTAR* revealed strong flares reaching up to $\approx 1.2 \times 10^{34}$ erg s $^{-1}$ (3–79 keV), as well as the same peculiar drops in flux (Tendulkar et al. 2014). This behavior bears close resemblance to that observed in PSR J1824–2452I (Linares et al. 2014) and XSS J12270–4859 (de Martino et al. 2010, 2013) in their low-luminosity LMXB states.

In Archibald et al. (2014), we established that despite PSR J1023+0038 existing at a luminosity level typical of quiescent LMXBs, active accretion onto the neutron star surface appears to be occurring on a regular basis as evidenced by the detection of coherent X-ray pulsations. Herein, we build upon this finding with a more in-depth analysis of the same *XMM-Newton* data set, which is augmented by an array of coordinated multi-wavelength observations of PSR J1023+0038. This study provides the most complete observational picture to date of the LMXB state of the PSR J1023+0038 system and, arguably, transition millisecond pulsar systems in general. The work is organized as follows. In §2, we summarize the observations and data analysis. In §3, we focus on the X-ray variability, while in §4 we focus on its statistical properties. We discuss the X-ray pulsations in §5 and summarize the spectroscopic analysis of the X-ray emission in §6. We describe the results of the optical photometry and spectroscopy in §7 and §8. We present the results of our radio imaging and timing observations in §9 and §10. Finally, in §11 we provide a discussion and offer conclusions in §12.

2. OBSERVATIONS AND DATA REDUCTION

Tables 1 and 2 summarize all X-ray, UV/optical, and radio observations presented in this paper, while Figure 1 shows a visual timeline of this multi-wavelength observing campaign, arranged around two *XMM-Newton* observations conducted in 2013 November and 2014 June.

2.1. X-ray Observations

2.1.1. XMM-Newton EPIC

PSR J1023+0038 was observed with *XMM-Newton* starting on 2013 November 10 in a 134-ks exposure (ObsID 0720030101). It was revisited on 2014 June 10 for 115 ks (ObsID 0742610101). For both observations, the European Photon Imaging Camera (EPIC) pn instrument (Strüder et al. 2001) was configured for fast timing mode, which permits a 30 μ s time resolution at the cost of one imaging dimension. To minimize the effect of pile up both EPIC MOS cameras (Turner et al. 2001) were used in small window mode with 0.3 s time resolution. For all three detectors, the thin optical blocking filter was in place.

The data reduction and extraction of the EPIC data were carried out using the Science Analysis Software (SAS⁹) version `xmmsas_20130501_1901-13.0.0`. The observations were filtered using the recommended flag and pattern values. For the X-ray variability analysis, background-subtracted and exposure-corrected light curves were obtained with the `epiclccor` tool in SAS. Owing to the bright nature of PSR J1023+0038 in its current state, when constructing binned light curves it was not necessary to remove time intervals of high background flaring. To maximize the sensitivity to pulsations, for the fast timing photon lists, we determined time ranges corresponding to soft proton flares by thresholding a 10-s binned light curve extracted from an off-source region; photons arriving during these time ranges were not used in the pulsed flux and profile analyses.

The pn fast timing mode data were extracted using a region of width 6.5 pixels in the imaging (RAWX) direction centered on row 37. This translates to an angular size of 27'', which encircles $\sim 87\%$ of the energy from

⁹ The *XMM-Newton* SAS is developed and maintained by the Science Operations Centre at the European Space Astronomy Centre and the Survey Science Centre at the University of Leicester.

TABLE 1
LOG OF OBSERVATIONS OF PSR J1023+0038 DURING 2013 NOVEMBER 10–12.

Telescope/ Instrument	Start time (MJD)	Duration (s)	Band	Mode
<i>XMM-Newton</i> /EPIC pn	56606.69084	136981	0.3–10 keV	Fast timing
<i>XMM-Newton</i> /EPIC MOS1	56606.66645	136942	0.3–10 keV	Small Window
<i>XMM-Newton</i> /EPIC MOS2	56606.66696	134893	0.3–10 keV	Small Window
<i>Swift</i> /XRT	56606.83056	1161	0.3–10 keV	Fast
...	56607.11389	2312	0.3–10 keV	Fast
...	56608.04375	1138	0.3–10 keV	Fast
...	56609.84792	1098	0.3–10 keV	Fast
<i>XMM-Newton</i> /OM	56606.67079	4656	<i>B</i>	Image Fast
...	56606.72470	4720	<i>B</i>	Image Fast
...	56606.77935	4720	<i>B</i>	Image Fast
...	56606.83400	4720	<i>B</i>	Image Fast
...	56606.88866	4720	<i>B</i>	Image Fast
...	56606.94403	4656	<i>B</i>	Image Fast
...	56606.99794	4720	<i>B</i>	Image Fast
...	56607.05259	4720	<i>B</i>	Image Fast
...	56607.10725	4720	<i>B</i>	Image Fast
...	56607.16190	4720	<i>B</i>	Image Fast
...	56607.21727	4656	<i>B</i>	Image Fast
...	56607.27118	4720	<i>B</i>	Image Fast
...	56607.32583	4720	<i>B</i>	Image Fast
...	56607.38049	4720	<i>B</i>	Image Fast
...	56607.43514	4720	<i>B</i>	Image Fast
...	56607.49051	4656	<i>B</i>	Image Fast
...	56607.54442	4720	<i>B</i>	Image Fast
...	56607.59907	4720	<i>B</i>	Image Fast
...	56607.65373	6520	<i>B</i>	Image Fast
...	56607.72921	4720	<i>B</i>	Image Fast
...	56607.78458	4656	<i>B</i>	Image Fast
...	56607.83850	6520	<i>B</i>	Image Fast
...	56607.91398	4720	<i>B</i>	Image Fast
...	56607.96863	4720	<i>B</i>	Image Fast
...	56608.02329	4720	<i>B</i>	Image Fast
...	56608.07866	2592	<i>B</i>	Image Fast
...	56608.10868	2656	<i>B</i>	Image Fast
...	56608.13944	2656	<i>B</i>	Image Fast
...	56608.17021	2656	<i>B</i>	Image Fast
...	56608.20097	2656	<i>B</i>	Image Fast
<i>Swift</i> /UVOT	56606.83056	1158	<i>UVW1</i>	Fast
...	56607.11389	2307	<i>UVW1</i>	Fast
...	56608.04375	1138	<i>UVW1</i>	Fast
...	56609.84792	1096	<i>UVW1</i>	Fast
VLT/X-Shooter	56608.31458	3480	3000–25000 Å	Spectroscopy
VLA	56606.68070	7200	4.5–5.5 GHz	Imaging
...	56606.68070	7200	6.5–7.5 GHz	Imaging
...	56607.57380	3600	2.0–4.0 GHz	Imaging
LOFAR	56607.18198	17818.8	0.139–0.162 GHz	Imaging
e-EVN	56609.08333	28800	4.93–5.05 GHz	Imaging
Lovell	56607.06111	41640	1.3–1.7 GHz	Timing
...	56608.05833	15360	1.3–1.7 GHz	Timing
WSRT	56607.02581	7190	2.20–2.34 GHz	Timing
...	56607.11135	3579	0.31–0.38 GHz	Timing
...	56607.15509	3580	2.20–2.34 GHz	Timing
...	56607.19885	2380	0.31–0.38 GHz	Timing
...	56608.02303	7190	2.20–2.34 GHz	Timing
...	56608.10857	3579	0.31–0.38 GHz	Timing
...	56608.15231	3580	2.20–2.34 GHz	Timing
...	56608.19606	3580	4.83–4.97 GHz	Timing
...	56608.23981	3580	2.20–2.34 GHz	Timing

the point source at 1.5 keV. The MOS1/2 source events were obtained from circular regions of radius $36''$ (limited by the size of the small imaging window), which enclose $\sim 88\%$ of the total point source energy at ~ 1.5 keV. Due to the occasional instances of relatively high source count rates ($\sim 4 - 5$ counts s^{-1}), the MOS1/2 instruments are susceptible to photon pile-up. Pile-up occurs when two or more events occur during a single read-out interval and are registered as a single event with energy approximately equal to the sum of the individual event energies

(Davis 2001). This can result in artificial hardening of the intrinsic source spectrum and loss of source events. To diagnose the impact of pile-up, we used the SAS tool *epatplot*. Based on this, we determined that pile-up is negligible.

For the variability and pulsation analyses, the photon arrival times were translated to the solar system barycenter using the DE405 solar system ephemeris and the best known astrometric position of the pulsar from Deller et al. (2012).

TABLE 2
LOG OF OBSERVATIONS OF PSR J1023+0038 DURING 2014 JUNE 10–11.

Telescope/ Instrument	Start time (MJD)	Duration (s)	Band	Mode
<i>XMM-Newton</i> /EPIC pn	56818.18118	116726	0.3–10 keV	Fast timing
<i>XMM-Newton</i> /EPIC MOS1	56818.15704	13962	0.3–10 keV	Small Window
...	56818.33610	103225	0.3–10 keV	Small Window
...	56819.57051	2913	0.3–10 keV	Small Window
<i>XMM-Newton</i> /EPIC MOS2	56818.15756	118502	0.3–10 keV	Small Window
...	56819.57433	7301	0.3–10 keV	Small Window
<i>Swift</i> /XRT	56819.16666	2763	0.3–10 keV	Fast
<i>XMM-Newton</i> /OM	56818.16030	3456	<i>B</i>	Image Fast
...	56818.20032	3520	<i>B</i>	Image Fast
...	56818.24109	3520	<i>B</i>	Image Fast
...	56818.28185	3520	<i>B</i>	Image Fast
...	56818.32262	3520	<i>B</i>	Image Fast
...	56818.36410	5256	<i>B</i>	Image Fast
...	56818.42495	3520	<i>B</i>	Image Fast
...	56818.46572	3520	<i>B</i>	Image Fast
...	56818.50648	3520	<i>B</i>	Image Fast
...	56818.54725	3520	<i>B</i>	Image Fast
...	56818.58873	3456	<i>B</i>	Image Fast
...	56818.62875	3520	<i>B</i>	Image Fast
...	56818.66951	3520	<i>B</i>	Image Fast
...	56818.71028	3520	<i>B</i>	Image Fast
...	56818.79271	3520	<i>B</i>	Image Fast
...	56818.79252	3456	<i>B</i>	Image Fast
...	56818.83255	3520	<i>B</i>	Image Fast
...	56818.87331	3520	<i>B</i>	Image Fast
...	56818.91407	3520	<i>B</i>	Image Fast
...	56818.95484	3520	<i>B</i>	Image Fast
...	56818.99632	3456	<i>B</i>	Image Fast
...	56819.03634	3520	<i>B</i>	Image Fast
...	56819.07711	5320	<i>B</i>	Image Fast
...	56819.13870	3520	<i>B</i>	Image Fast
...	56819.17947	3520	<i>B</i>	Image Fast
...	56819.22095	3456	<i>B</i>	Image Fast
...	56819.26097	3520	<i>B</i>	Image Fast
...	56819.30174	3520	<i>B</i>	Image Fast
...	56819.34250	3520	<i>B</i>	Image Fast
...	56819.38326	3520	<i>B</i>	Image Fast
...	56819.42475	3456	<i>B</i>	Image Fast
...	56819.46477	3520	<i>B</i>	Image Fast
...	56819.50553	3520	<i>B</i>	Image Fast
...	56819.54630	3520	<i>B</i>	Image Fast
...	56819.58706	3520	<i>B</i>	Image Fast
<i>Swift</i> /UVOT	56819.16666	2761	<i>UVW2</i>	Fast
WSRT	56819.52118	10800	1.30–1.46 GHz	Timing
...	56819.64826	3600	2.20–2.34 GHz	Timing
...	56819.69201	3600	0.31–0.38 GHz	Timing

2.1.2. *XMM-Newton* RGS

We extracted and processed the Reflection Grating Spectrometer (RGS) data using the recommended SAS analysis procedures. The extracted grating spectra show no obvious emission or absorption features. The combination of lower count rate compared to the EPIC data and the elevated background of the dispersed spectrum results in a low signal-to-noise ratio. For this reason we do not make use of the RGS data in our analysis.

2.1.3. *Swift* XRT

Swift has been used to regularly monitor the long-term behavior of PSR J1023+0038 since 2013 October (Patruno et al. 2014; Takata et al. 2014; Coti Zelati et al. 2014). It observed the binary on 2013 November 10–13 November 2013 and 2014 June 11 coincident with the *XMM-Newton* exposures. The XRT was operated in photon-counting mode (enabling 2.5-s time resolution) in all exposures. Due to the significantly lower sensitivity of the XRT relative to the

XMM-Newton EPIC cameras, we do not use these data in the analysis below. We only note that, as expected, the observed count rates are in full agreement with those observed with *XMM-Newton*.

2.2. Optical/UV Photometry

2.2.1. *XMM-Newton* OM

The *XMM-Newton* Optical Monitor (OM; Mason et al. 2001) was used with the *B* filter, which has a band pass between 3800 and 5000 Å centered on 4392 Å, and was employed in “Image Fast” mode to provide high time resolution and photon counting capabilities. The data was obtained in 30 exposures, typically of 4.7 ks each, in the 2013 November observations and 35 exposures in the 2014 July observation, typically of 3.5 ks each (see Tables 1 and 2). The background-subtracted photometric *B* filter data from the OM were extracted using the SAS `omfchain` pipeline script using the default set of parameters. Time bins of 10 s were chosen in order to examine

TABLE 3
LOG OF MDM OBSERVATORY TIME SERIES

Telescope	Date (UT)	Time (UT)	Filter	N_{exp}^a
1.3-m	2013 Dec 26	07:44–13:32	<i>B</i>	1598
1.3-m	2013 Dec 27	07:41–13:32	<i>B</i>	1606
1.3-m	2013 Dec 28	08:15–13:30	<i>B</i>	1445
1.3-m	2013 Dec 29	10:18–13:39	<i>BG38</i>	922
1.3-m	2014 Jan 3	08:33–13:36	<i>B</i>	1384
2.4-m	2014 Mar 22	06:52–09:41	<i>B</i>	670
2.4-m	2014 May 30	03:51–05:15	<i>B</i>	335

^a All exposures were 10 s.

the rapid variability in the system.

2.2.2. *Swift* UVOT

We use all data collected with the *Swift* Ultra-Violet/Optical Telescope (UVOT) during 2013 November 10–13 November and 2014 June 11. During the former, the UVOT was operated with the *UVW1* filter, which has a central wavelength of 2600 Å and a bandpass between 2200 and 4000 Å, while during the latter the *UVW2* filter, which has a central wavelength of 2246 Å and a bandpass between 1800 and 2600 Å, was in place.

We reduced the data using the UVOT pipeline in FT00LS and applying standard event screening criteria. We extracted source events for each observation using circular regions with radius 5'' and by using the best source position available (Deller et al. 2012). The resulting time series were barycentered to allow an investigation of correlated behavior with the contemporaneous *XMM-Newton* light curves.

2.2.3. MDM

In this paper, we also present time-series optical photometry obtained on seven nights during the 2013–2014 observing season using the MDM Observatory’s 1.3-m McGraw-Hill telescope or 2.4-m Hiltner telescope on Kitt Peak (see Table 3 for a summary). In all cases the detector was the thinned, backside illuminated SITE CCD “Templeton”. It has 1024×1024 pixels, with a scale of $0.''509 \text{ pixel}^{-1}$ on the 1.3-m, and $0.''275 \text{ pixel}^{-1}$ on the 2.4-m. In order to reduce the readout time, the CCD was windowed down and the pixels were binned 2×2 . All exposures were 10 s, with a read/prep time of 3 s, resulting in a 13-s cadence. All but one of the light curves used the *B* filter. On 2013 December 29 we used a broadband *BG38* filter. Differential photometry was performed with respect to a field star calibrated by Thornstensen & Armstrong (2005) that has $B = 15.51$ and $V = 14.86$, the latter used to approximate a magnitude in the *BG38* filter. A heliocentric correction was applied to the observing times.

2.3. Optical Spectroscopy

PSR J1023+0038 was observed with the X-SHOOTER instrument at the European Southern Observatory (ESO) Very Large Telescope (VLT) in Paranal, Chile. X-SHOOTER is a medium resolution ($R = 4000$ to 7000) spectrograph covering a wavelength range from 3000 Å to 2.5 μm. Two exposures were obtained on 2013 November 12 between 07:55UT and 08:30UT, shortly after the

end of the 2013 November *XMM-Newton* observation. The exposure times were 600 s in the UVB arm (3000–5595 Å), 628.7 s in the VIS arm (5595 Å to 1.024 μm) and 2×300 s in the NIR arm (1.024–2.48 μm). The width of the slit was 1''0 in the UVB arm and 0''9 in the VIS and NIR arms. The observing conditions were good with 1''1 seeing. The obtained spectra were reduced and calibrated with standard ESO software tools (Reflex 2.6, X-Shooter pipeline 2.5.2).

2.4. Radio Timing Observations

For part of both the November 2013 and June 2014 observations, simultaneous radio data were acquired with either one, or both, of the Westerbork Synthesis Radio Telescope (WSRT) and the Lovell Telescope (LT) at Jodrell Bank Observatory (see Tables 1 and 2 for details). The WSRT observations were made at central frequencies of 350, 1380, 2273, and 4901 MHz and the LT observations were made at 1532 MHz. A detailed description of the observing systems can be found in Stappers et al. (2014).

2.5. Radio Imaging Observations

PSR J1023+0038 was targeted by the Karl G. Jansky Very Large Array (VLA) in B configuration for two hours on 2013 November 10, covering 4.5–5.5 and 6.5–7.5 GHz, and for one hour on 2013 November 11, covering 2.0–4.0 GHz.

The system was observed with the very long baseline interferometry technique (VLBI), with the European VLBI Network (EVN) in realtime e-VLBI mode on 2013 November 13 between 2:00–10:00 UT. The following telescopes of the e-EVN array participated: Jodrell Bank (MkII), Effelsberg, Hartebeesthoek, Medicina, Noto, Onsala (25m), Shanghai (25m), Toruń, Yebes, and the phased-array WSRT.

PSR J1023+0038 was also observed by the Low Frequency Array (LOFAR; van Haarlem et al. 2013) for 5 hours on 2013 November 11, between 04:22–09:19 UT, with bandwidth spanning the frequency range 138.5–161.7 MHz. All Dutch stations were included, for a total of 60 correlated elements.

A more detailed description of the calibration, data reduction and analysis procedures of all radio imaging observations — including a much more extensive radio continuum monitoring campaign — is provided in Deller et al. (2014).

3. X-RAY VARIABILITY

Figures 2 and 3 show the total exposure-corrected, background-subtracted *XMM-Newton* EPIC X-ray light curves in the 0.3–10 keV band, obtained by combining the data from the pn, MOS1, and MOS2 during the periods when all three telescopes acquired data simultaneously. The large-amplitude variability is obvious and is reminiscent of the behavior seen in the *Swift* XRT (Patruno et al. 2014) and *NuSTAR* (Tendulkar et al. 2014) observations of PSR J1023+0038 from 2013 October. During both *XMM-Newton* observations, most of the time is spent in the “high” mode¹⁰, with a typical to-

¹⁰ For the sake of clarity, we adopt the following nomenclature: we refer to the three distinct X-ray flux levels as “modes”, while we refer to the long-term radio pulsar and LMXB intervals as “states”.

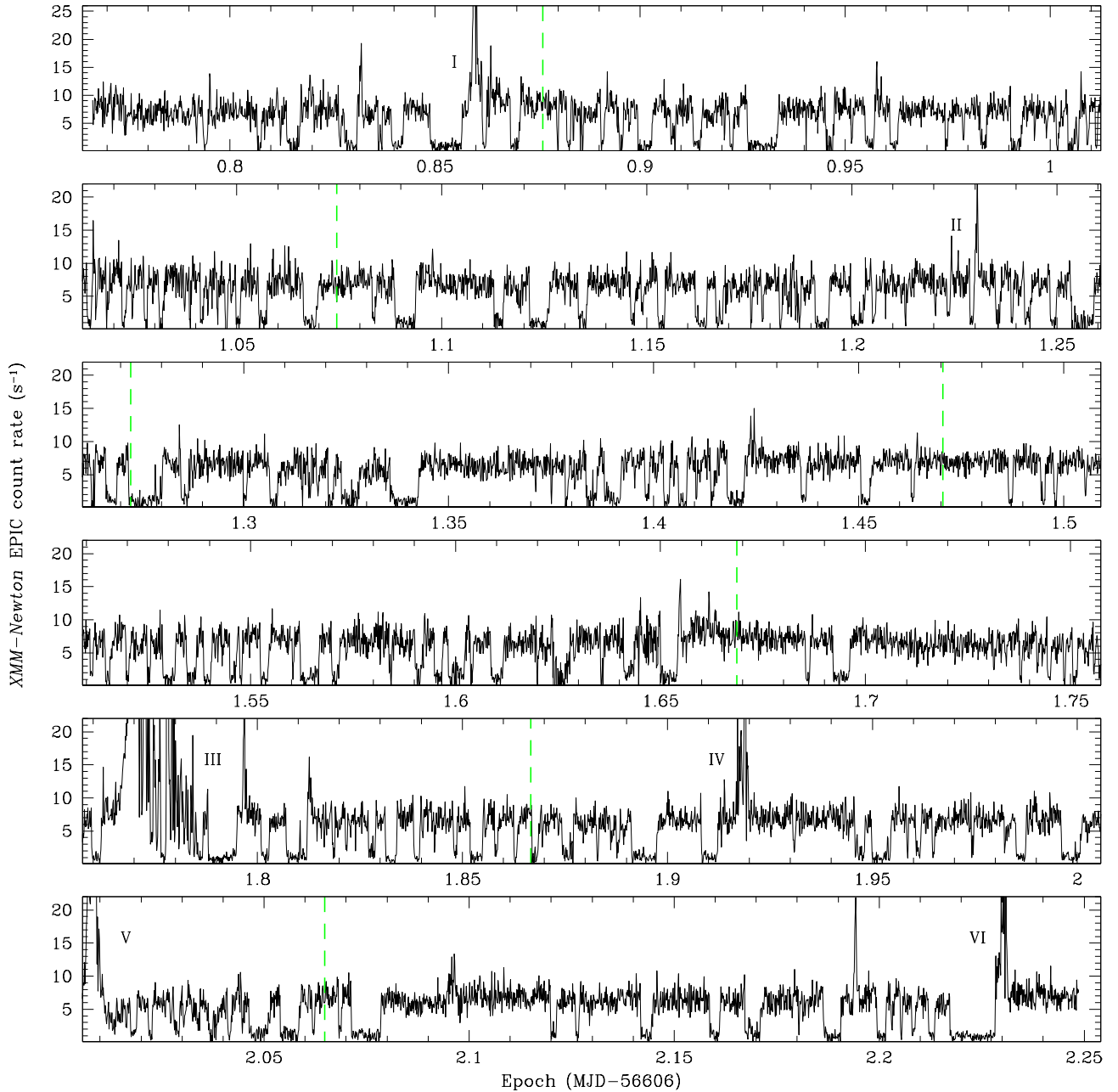


FIG. 2.— Total background-subtracted and exposure-corrected *XMM-Newton* EPIC lightcurve of PSR J1023+0038 in the 0.3–10 keV band from ObsID 0720030101, acquired during 2013 November 10–12. The vertical dotted lines mark the times of orbital phase $\phi_b = 0.25$ of the binary. The Roman numerals mark the six prominent flares.

tal EPIC count rate of ~ 7 counts s^{-1} (0.3–10 keV). The emission drops out unpredictably to the “low” mode with count rate ~ 1 counts s^{-1} with very rapid ingress and egress (~ 10 –30 s).

Sporadic, intense X-ray flares (labeled by the Roman numerals in Figures 2 and 3), reaching up to nearly ~ 60 counts s^{-1} , occur on average every few hours, and exhibit diverse morphologies and durations. Some flares last less than a minute (e.g. II), while others (e.g. III, IX, and XI) last up to ~ 45 minutes. The long-duration flares exhibit a great deal of intricate structure. Specifically, throughout flares III and XI, there are a number of rapid drops in count rate that occasionally reach down to

the levels of the low flux mode. In both *XMM-Newton* observations, the recurrence time between X-ray flares is comparable (~ 20 ks), with six prominent flares (which we define as those with peak rates exceeding 25 counts s^{-1}) in each observation.

In the disk-free, radio pulsar state, PSR J1023+0038 exhibited pronounced orbital-phase-dependent X-ray flux modulations (Archibald et al. 2010; Bogdanov et al. 2011). Although in the light curves shown in Figures 2 and 3 there is no obvious periodic behavior (see §4), in principle, orbital modulation may still be present in one of the X-ray flux modes. To investigate this possibility, we separately extracted the emission from the high, low,

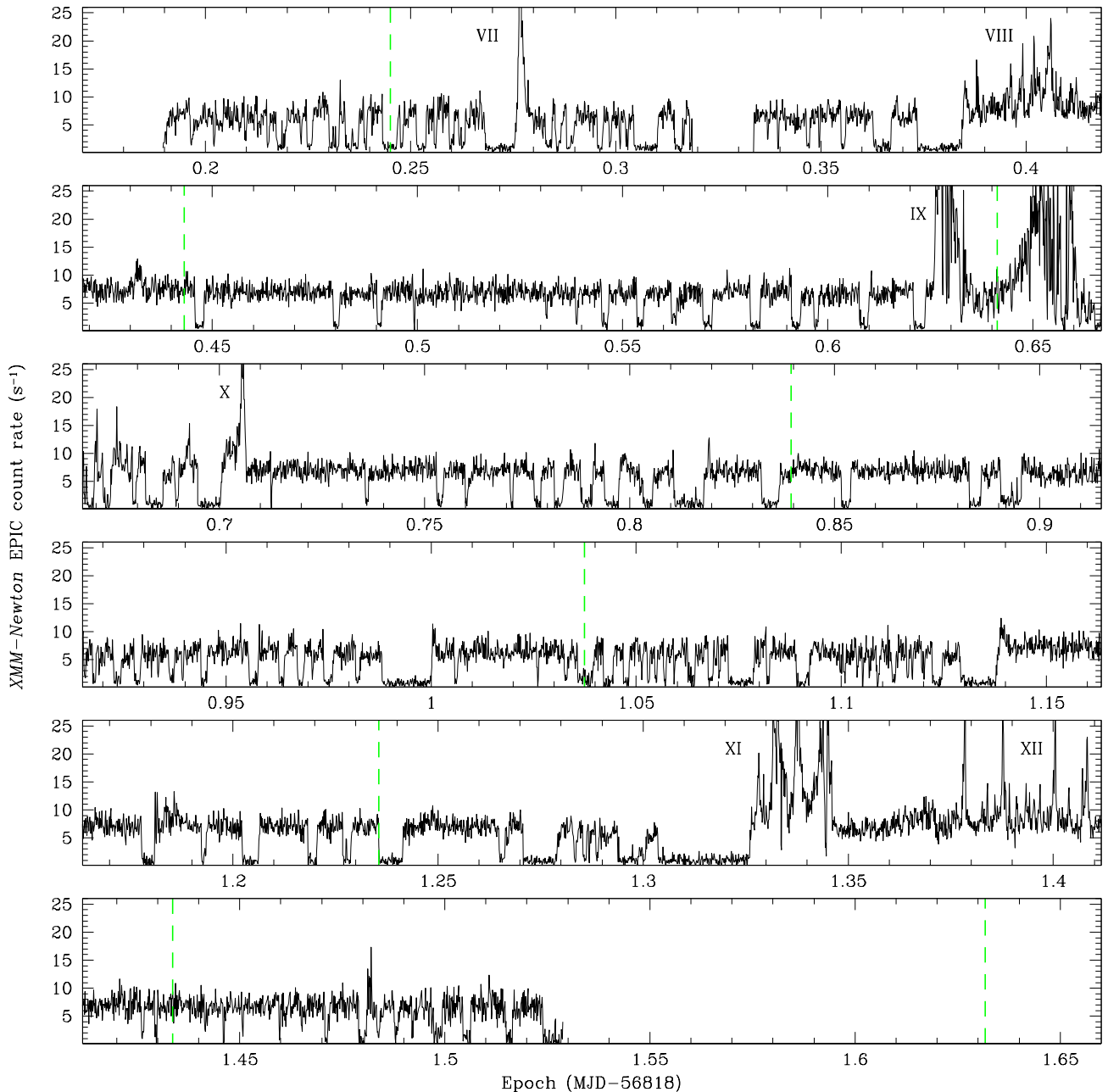


FIG. 3.— Same as Figure 2 but for ObsID 0742610101, acquired during 2014 June 10–11.

and flare modes and folded them at the orbital period. We do not find evidence for orbital modulation of the X-ray brightness during any of the three modes.

Li et al. (2014a) have reported evidence for periodicity at 3130 s in the *NuSTAR* data set of PSR J1023+0038. We have examined both *XMM-Newton* observations in search of a similar signal but find no evidence for it. In addition, we are not able to reproduce this result using the *NuSTAR* data presented in Tendulkar et al. (2014).

4. STATISTICAL ANALYSIS OF THE X-RAY VARIABILITY

We performed a statistical analysis of the low, high, and flare X-ray flux modes to understand their temporal properties and identify any correlations between

them. We followed the same methodology as the analysis performed on the *NuSTAR* data of PSR J1023+0038 in Tendulkar et al. (2014). We use the combined background-subtracted and exposure corrected EPIC 0.3–10 keV data binned with 10-s bins shown in Figures 2 and 3. The 10-s bins were chosen to ensure sufficient photon statistics in the low mode bins and in the mode transitions.

Figure 5 shows the distribution of count rates throughout the 2013 November (solid black line) and 2014 June (dashed red line) observations. The bi-modality in the distribution is immediately apparent, with the low and high modes clearly seen as peaks at $\approx 1 \text{ counts s}^{-1}$ and $\approx 7 \text{ counts s}^{-1}$ respectively for both epochs. In both in-

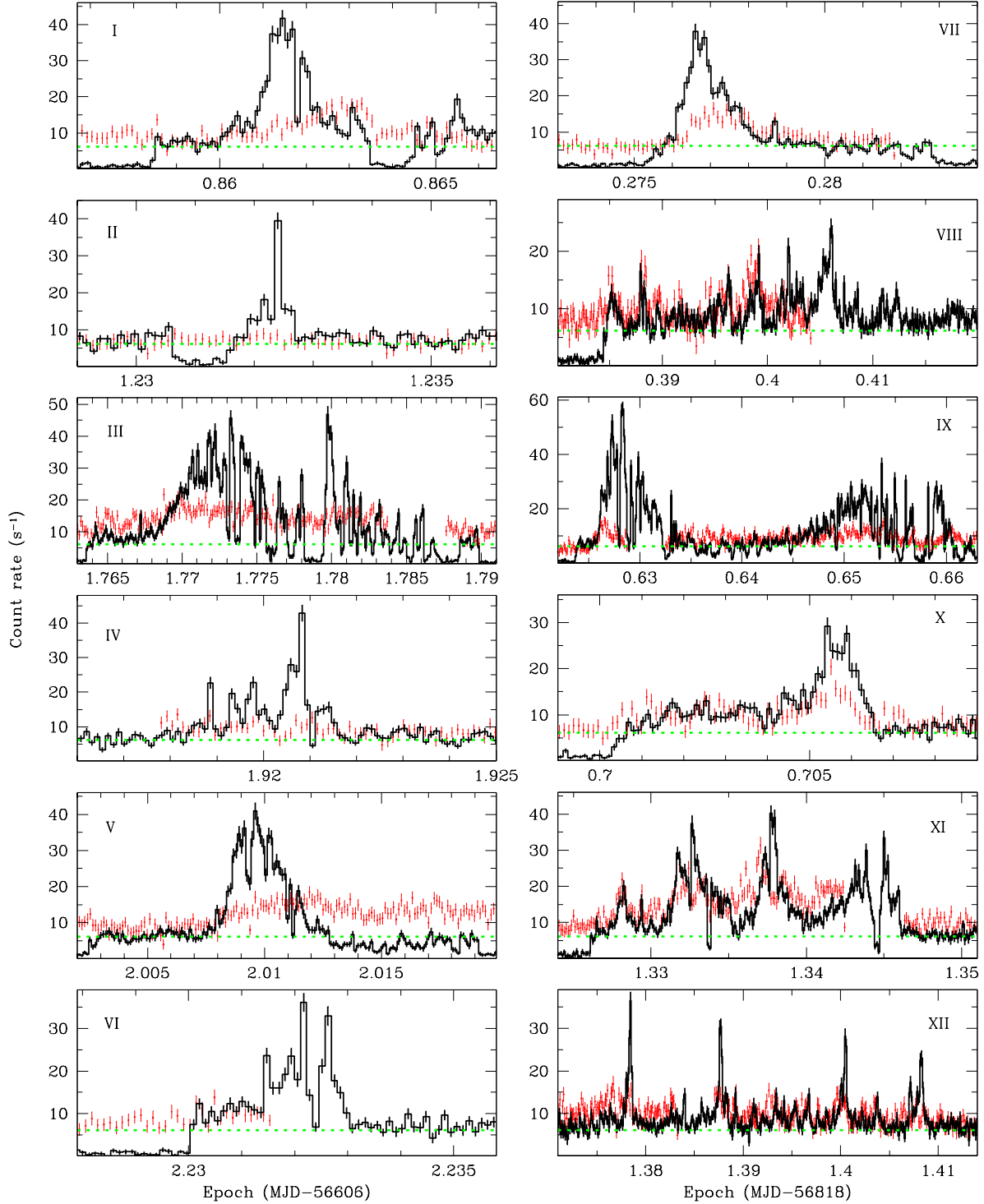


FIG. 4.— A detailed view of the prominent flares observed with *XMM-Newton* in 2013 November (left) and 2014 June (right). The Roman numerals correspond to those in Figures 2 and 3. The red points show the photometric *B* filter data from the *XMM-Newton* OM in units of counts s^{-1} binned at a 10 s resolution. For reference, the dotted (green) horizontal line shows the mean X-ray flux level in the 0.3–10 keV range over the entire observation.

stances, the distribution of count rates for the low and high mode are consistent with what is expected from a Poisson distribution. The minimum of the distribution between the two states occurs at approximately $3.1 \text{ counts s}^{-1}$.

To cleanly differentiate between the two modes and

the transitions between them, we define a “grey area” (hatched region in Figure 5) between $2.1 \text{ counts s}^{-1}$ and $4.1 \text{ counts s}^{-1}$. These limits were chosen to be symmetrical around the minimum of the distribution, though because of the inherent count-rate errors in each lightcurve bin, the exact values of these thresholds is not critical

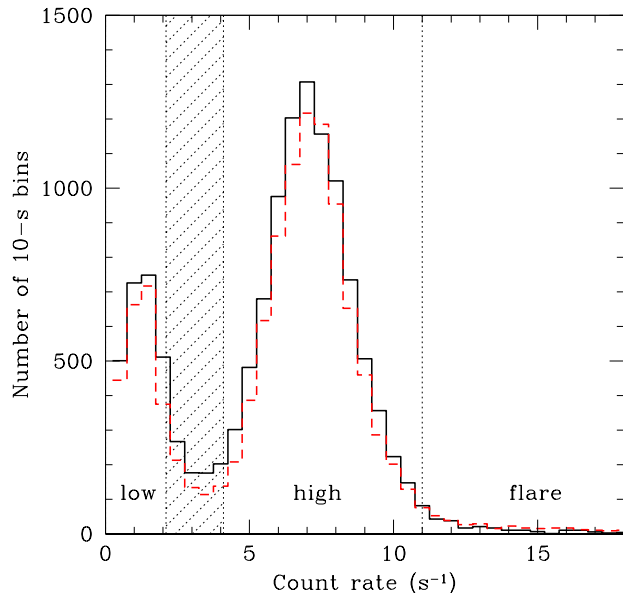


FIG. 5.— Distribution of count rates obtained from the 10-s binned lightcurves from the 2013 November (solid black line) and 2014 June (dashed red line) *XMM-Newton* data. We define the region between 0 counts s^{-1} and 2.1 counts s^{-1} as the low mode, while the zone between 4.1 counts s^{-1} and 11 counts s^{-1} is the high mode. The hatched region denotes the “grey area” or transition region defined in the text.

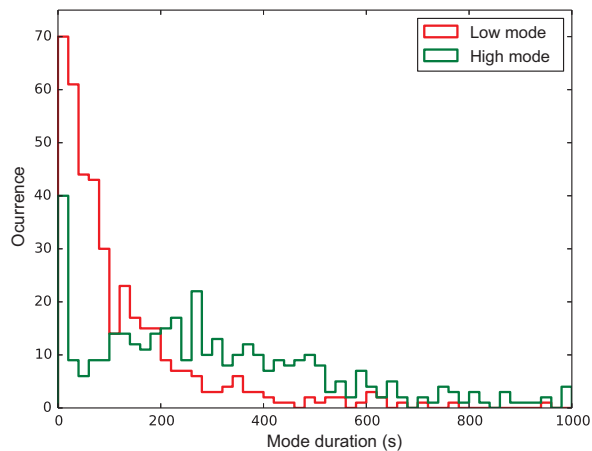


FIG. 6.— Histogram of the durations of low (solid red line) and high modes (solid green line). The data from 2013 November and 2014 June are combined. While the longest high mode instance observed is ≈ 7000 s long, this histogram is truncated to durations < 1000 s to improve visibility.

to the analysis presented below¹¹. In particular, varying the thresholds by $\pm 0.3 s^{-1}$ results in a difference of less than 1% in the number of transitions. The red and green zones in Figure 5 show all the thresholds for low and high states. In the analysis that follows, the flare mode intervals were removed from the lightcurves by excluding intervals with rates in excess of 11 counts s^{-1} .

We use a bi-stable comparator¹² to define the transi-

¹¹ In Archibald et al. (2014), slightly different criteria were used in defining the modes. Nevertheless, the two procedures result in negligible differences ($\lesssim 1\%$).

¹² In the field of electronics this is known as a Schmitt trigger.

tions between the modes as follows. A low-high transition is defined when the count rate crosses from the red zone to the green zone shown in Figure 5 and reverse for the high-low transition. If the light curve varies from the “low” region to the hatched region and returns back to the “low” region, the lightcurve mode is maintained as low and a transition is not registered. Similarly, a variation from the “high” zone to the hatched region and back to the “high” zone is maintained as a high mode.

Using this comparator algorithm, we counted 237 low-high and high-low transitions in the 2013 November data and 172 low-high transitions and 171 high-low transitions in the 2014 June data. We measured the durations of the low and high modes as the number of lightcurve bins between the end of the previous transition and the beginning of the next transition. The duration of the transition itself was estimated as the number of light curve bins spent in the “grey area”.

Figure 6 shows the distribution of durations of the low (red line) and high (green line) mode based on the combined 2013 November and 2014 June data sets. The histogram is truncated to show only durations shorter than 1000s although the longest continuous high mode interval was 6910s in 2014 June and the longest low mode lasted 1930s, also in 2014 June. We find that the low mode exists for $\approx 22\%$ of the total observation time during 2013 November 10-12 and $\approx 21\%$ during 2014 June 10-11 observations. As shown in Figure 6, the high mode exists for significantly longer durations than the low mode. The distribution of low mode durations can be very approximately modeled as a power law with a slope of $\Gamma = 1.3$.

We also looked for correlations or patterns between durations of consecutive modes. There is no perceptible pattern or correlation between the two modes, indicating a stochastic nature of the underlying physical mechanism responsible for the switches between the two. However, we do note that the modes last longer during 2014 June as compared to the durations in 2013 November, which suggests some long-term variation in behavior.

We have also investigated the distribution of the times of the low-high and high-low transitions for 2013 November and 2014 June. We find that 57% of the high-low transitions in 2013 November and 54% of those in 2014 June lasted < 10 s. In contrast, only 40% of the low-high transitions in 2013 November and 39% of those in 2014 June were < 10 s. Thus, based on this estimate, we find evidence that high-low transitions may be faster than the low-high transitions.

5. X-RAY PULSATIONS

As reported in Archibald et al. (2014), the *XMM-Newton* data revealed coherent modulations at the pulsar spin period in both the 2013 November and 2014 June observations. Intriguingly, the pulsations occur just in the high flux mode, with a pulsed fraction of 8% (0.3–10 keV). The profile is clearly double-peaked, with a $\sim 180^\circ$ separation in rotational phase, with each peak presumably corresponding to emission from one of the diametrically opposite magnetic polar caps of the neutron star.

Here we examine the energy dependence of the high mode X-ray pulse profiles as well as any spectral variations as a function of spin phase. The method for extracting the pulse profiles is given in Archibald et al. (2014).

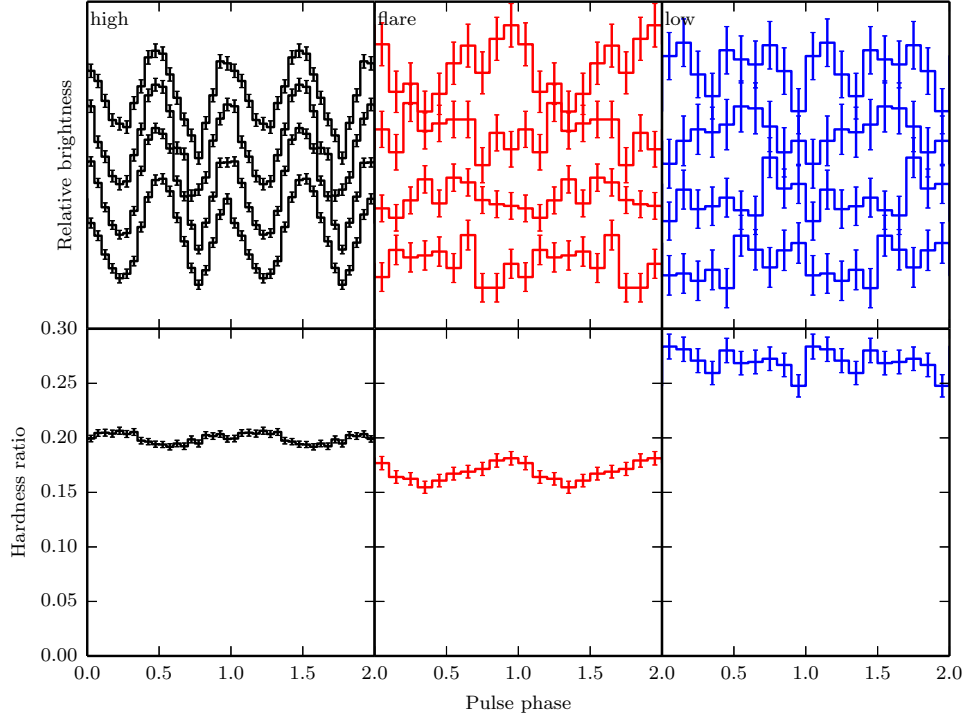


FIG. 7.— Top panels: Normalized pulse profiles of PSR J1023+0038 in the 0.3–0.7, 0.7–1.5, 1.5–3, and 3–10 keV bands (from bottom to top, respectively) in the three X-ray flux modes: high (left), flare (middle), and low (right). Bottom panels: Hardness ratios of the three pulse profiles with the 1–10 keV counts divided by the counts in the 0.3–1 keV band. The curves plotted on top of the data were obtained by Fourier smoothing (see Archibald et al. 2014, for details).

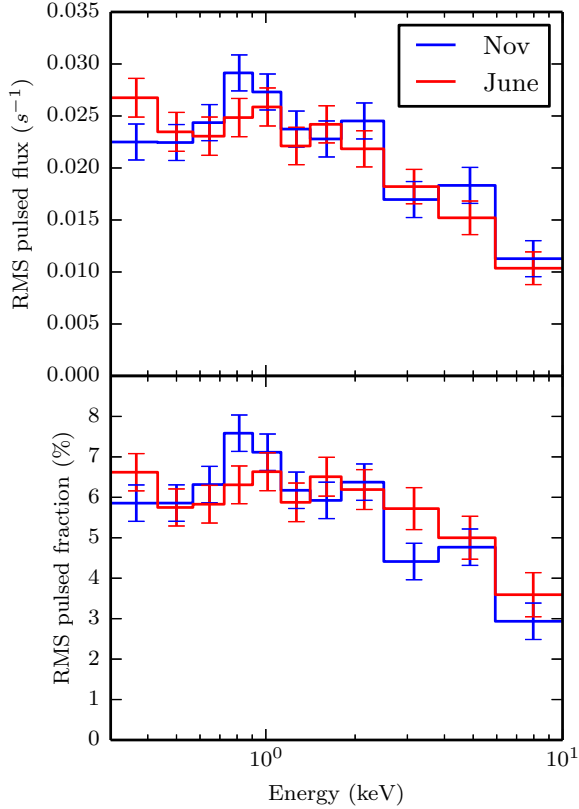


FIG. 8.— Pulsed flux and fraction as a function of energy for both November and June observations. The flux curve (top), expressed in instrument counts per second, is dominated by instrumental sensitivity, but only the relatively low background distorts the shape of the pulsed fraction curve (bottom).

TABLE 4
RESULTS OF ABSORBED POWER-LAW FITS OF THE *XMM-Newton* SPECTRA OF PSR J1023+0038.

Mode	N_{H} (10^{20} cm^{-2})	Γ	L_X^{b} ($10^{33} \text{ erg s}^{-1}$)	χ^2/dof
2013 November 10-12 (ObsID 0720030101)				
Flare	2.7(9)	1.65(4)	10.8(2)	0.98/321
High	3.1(2)	1.71(1)	3.17(2)	1.23/902
Low	2.6(11)	1.80(5)	0.54(1)	1.02/281
Flare ^c	3.1(2)	1.66(2)	10.9(2)	1.14/1506
High	...	1.71(1)	3.17(2)	...
Low	...	1.82(3)	0.54(1)	...
2014 June 10-11 (ObsID 0742610101)				
Flare	3.6(8)	1.76(3)	9.6(2)	1.02/373
High	3.1(2)	1.75(1)	3.06(2)	1.31/870
Low	2.4(12)	1.77(6)	0.45(1)	0.96/206
Flare ^c	3.1(2)	1.74(2)	9.6(1)	1.18/1452
High	...	1.75(1)	3.06(2)	...
Low	...	1.80(4)	0.46(1)	...

^a The numbers in parentheses show the 90% confidence level uncertainties in the last digit of the quoted best-fit values.

^b Luminosity in the 0.3–10 keV band assuming the parallax distance of 1.37 kpc (Deller et al. 2012).

^c Fits performed jointly on the spectra of all three modes with a tied value of N_{H} .

The top right panel of Figure 7 shows the high mode pulse profile in four energy bands (0.3–0.7, 0.7–1.5, 1.5–3, and 3–10 keV) obtained by aligning the total profiles from the two individual observations via cross-correlation (see Archibald et al. 2014, for details). The hardness ratio of the high mode exhibits a subtle spectral softening in the trailing edge of the stronger pulse. For reference, we also show the flare and low mode data folded using the

TABLE 5
MULTI-COMPONENT MODEL FITS OF THE HIGH MODE *XMM-Newton* SPECTRA OF PSR J1023+0038.

Model ^a	N_{H} (10^{20} cm^{-2})	Γ	T_{eff} (10^6 K)	R_{eff} (km)	$L^{\infty}/L_{\text{Edd}}$	$L_{X,PL}^b$ ($10^{33} \text{ erg s}^{-1}$)	L_X^b ($10^{33} \text{ erg s}^{-1}$)	χ^2/dof
2013 November 10-12 (ObsID 0720030101)								
<i>powerlaw + nsa</i> ^c	2.5(6)	1.59(3)	1.49(21)	$2.9^{+2.6}_{-1.9}$...	3.00(4)	3.18(3)	1.12/900
<i>powerlaw + zamp</i>	2.5(5)	1.60(3)	-4.6(2)	3.02(4)	3.18(3)	1.12/900
2014 June 10-11 (ObsID 0742610101)								
<i>powerlaw + nsa</i>	2.3(6)	1.60(3)	1.45(18)	$3.3^{+2.7}_{-1.9}$...	2.85(4)	3.06(3)	1.15/868
<i>powerlaw + zamp</i>	2.2(5)	1.61(3)	-4.6(2)	2.87(4)	3.06(3)	1.15/868

^a All uncertainties quoted are at a 90% confidence level.

^b Luminosity in the 0.3–10 keV band assuming the parallax distance of 1.37 kpc (Deller et al. 2012).

^c For the *nsa* model a neutron star with $M = 1.4 M_{\odot}$ and $R = 12 \text{ km}$ is assumed.

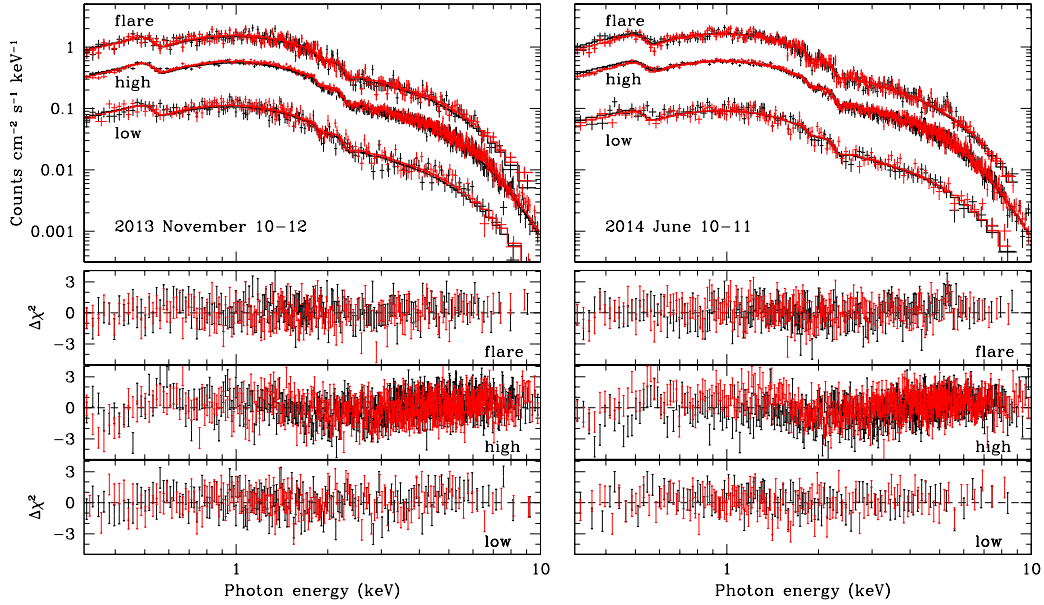


FIG. 9.— *XMM-Newton* MOS1 (black) and MOS2 (red) spectra from 2013 November (left) and 2014 June (right) of PSR J1023+0038 in the three distinct flux modes: flare, high, and low. In all instances, an absorbed power-law model is fitted. The bottom three panels show the best fit residuals for each mode. Note the broad residuals of the high mode spectra. See Table 3 for the best fit parameters.

same ephemeris, where no statistically significant pulsations are seen. The strongest, albeit marginal (with a single-trial significance of only $\sim 2\sigma$) signal is found above 3 keV for the flare mode, although it shows only single-peaked modulation.

As shown in Figure 8, the spectrum of the pulsations is similar to the spectrum of the source generally. This suggests that the pulsed and most of the unpulsed radiation are produced by the same process. It is possible that the pulsations decline above 5 keV but this cannot be conclusively established due to the limited photon statistics above this energy.

6. X-RAY SPECTROSCOPY

Previous studies of PSR J1023+0038 have established that the X-ray emission in the LMXB state is well-described by an absorbed power-law with spectral photon index of $\Gamma \approx 1.7$ with no substantial spectral changes despite the over one order of magnitude variation in flux (Patruno et al. 2014; Takata et al. 2014; Coti Zelati et al. 2014; Tendulkar et al. 2014). The large photon harvest of the *XMM-Newton* data presented here

allows us to identify any subtle differences in spectral properties between the three distinct flux modes: low, high, and flare. The corresponding spectra were obtained using selections based on the count rate ranges for the low and high modes determined in §4, while for the flares we choose a count rate cut of $\geq 15 \text{ counts s}^{-1}$ to minimize contamination from the high mode. Due to the relatively large uncertainties in the spectral calibration of pn timing mode data (see, e.g., Archibald et al. 2010; Bogdanov 2013), we only consider the MOS1/2 spectra in this analysis.

Table 4 summarizes the results of the power-law spectral fits for the three flux modes fitted in *XSPEC* (Arnaud 1996). We conducted the analysis in two ways: one with each mode fitted separately and the other with all three modes fitted jointly with a tied value of the hydrogen column density along the line of sight (N_{H}). In both instances, the fits suggest that the value of N_{H} is consistent among the three with no appreciable enhancement in the intervening absorbing column within the binary during any of the modes.

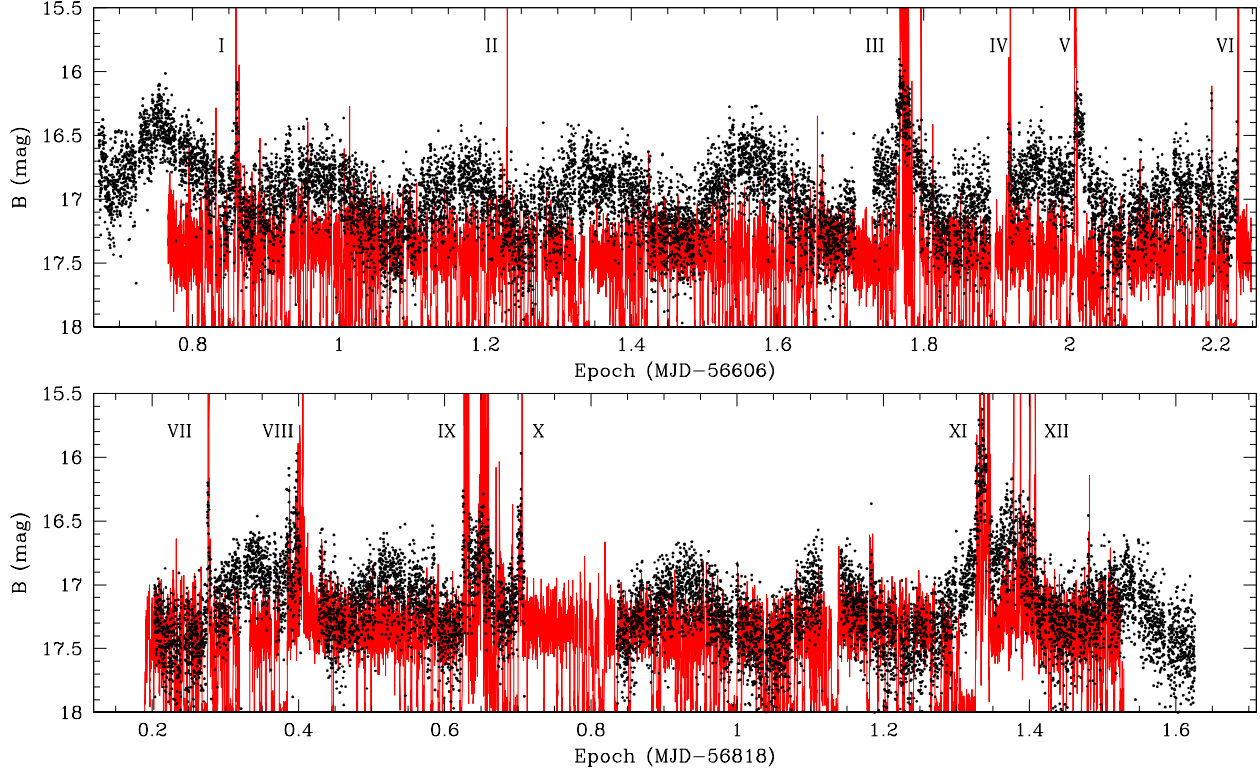


FIG. 10.— *XMM-Newton* OM fast mode lightcurve of PSR J1023+0038 in the *B* filter from 2013 November (top) and 2014 June (bottom). Each black point corresponds to a 10-s exposure. The error bars are omitted for the sake of clarity but are typically ± 0.2 mag. For reference, the 0.3–10 keV X-ray lightcurve (red) is plotted to show the relative alignment between the X-ray and optical flares. Gaps in the optical data are due to interruptions in exposure.

For the flare and low modes, the emission is well-described by an absorbed power-law in both observations. In contrast, the fits to the high mode spectra yield null hypothesis probabilities of 3×10^{-6} and 2×10^{-9} for the 2013 November and 2014 June data, respectively. This means that an absorbed power-law model alone does not provide an adequate representation of the high mode spectrum, which is also evident from the broad-band residuals shown in Figure 9. One likely explanation is the presence of a faint thermal (e.g., neutron star atmosphere) component since the X-ray pulsations imply accretion onto the neutron star, which may result in at least some superficial heating of the surface. To account for this emission we consider two models: *nsa*, a passive, weakly magnetized neutron star hydrogen atmosphere (Zavlin et al. 1996) and, *zamp*, a hydrogen atmosphere accreting at a low rate (Zampieri et al. 1995). For the latter, the spectrum is defined in terms of the observed accretion luminosity expressed in terms of the Eddington rate, assuming radiation from the entire surface of a neutron star with $M_{NS} = 1.4 M_{\odot}$ and $R_{NS} = 12.4$ km. The best fit parameters of the thermal component are consistent between the 2013 November and 2014 June observations (Table 5). The implied effective emission radii of the *nsa* model are smaller than the whole neutron star, consistent with emission from hot spots. The implied contribution of thermal radiation to the total luminosity (3–9%) is consistent with the pulsed fraction of the X-ray pulsations in the high mode. The implied luminosity from the *zamp* model is $2.5 \times 10^{-5} L_{\text{edd}}$, which translates to a thermal luminosity of $\sim 6 \times 10^{33}$ erg s $^{-1}$,

much greater than the implied thermal fraction. This arises due to the fact that the model considers emission from the entire surface, whereas the pulsations from PSR J1023+0038 indicate emission from a small portion of the surface. Although not strictly correct, adjusting the size of the emitting area to that obtained with the *nsa* model produces a value consistent with the thermal luminosity deduced from the spectral fits. While both composite models result in a reduction of the broad residuals relative to the pure power-law model, for both sets of observations the null hypothesis probabilities (7×10^{-3} and 1×10^{-3} , respectively) indicate fits that are formally not acceptable.

A possible explanation for the residuals in the high mode fits could be the presence of a complicated spectrum produced by three or more distinct emission components. An alternative interpretation involves small fluctuations of the power-law photon index during the high mode, which would result in a mean spectrum that is not well represented by a power-law with a single photon index. It is also possible that the flare and low state have similar residuals but due to the lack of photon statistics they are not as apparent.

The flux in the flare, high, and low modes appears to decrease by 11%, 3.5% and 16% between 2013 November and 2014 June. We have investigated whether this could be due to the choice of count rate cuts for the three flux modes. Using more conservative cuts produces similar results for the flux and photon index. Thus, the long-term flux changes of the modes appear to be intrinsic to

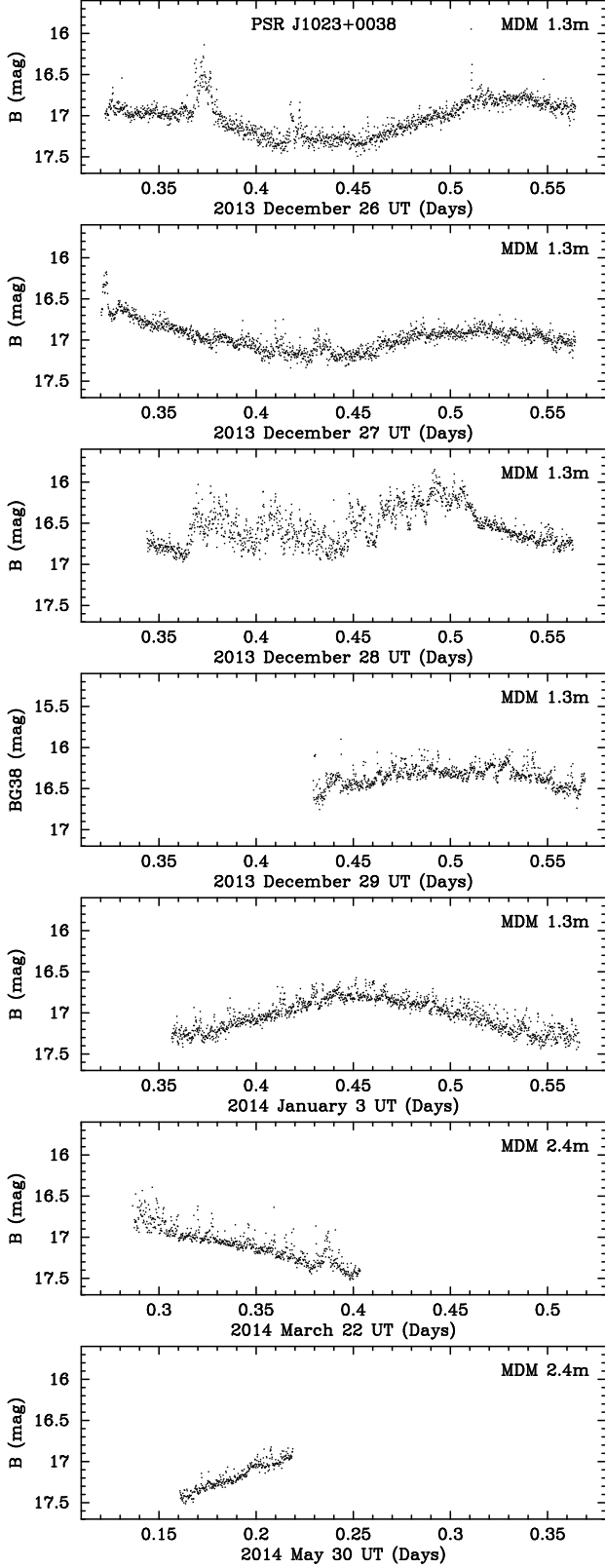


FIG. 11.— MDM light curves of PSR J1023+0038 with 13 s cadence, plotted as a function of heliocentric UT date. The orbital period of the binary is 0.198 d. Magnitudes are based on differential photometry with respect to a calibrated comparison star, as described in §2.2.3.

the system.

We note that for the case of the flare spectra the quoted luminosities represent time-averaged values. The peak luminosity, observed in flare IX, reaches a luminosity of $\approx 3 \times 10^{34}$ erg s $^{-1}$ (0.3–10 keV), assuming the same spectral shape as the mean flare spectrum.

7. OPTICAL/UV VARIABILITY

As noted by Halpern et al. (2013), in the optical the PSR J1023+0038 binary is ~ 1 magnitude brighter during the LMXB state than in the radio pulsar state. From the *XMM-Newton* OM and MDM photometric light curves (Figures 10 and 11) orbital modulation similar to the heating light curve observed during the radio pulsar state (Thornstensen & Armstrong 2005; Woudt et al. 2004) are also evident. However, the variations now appear more sinusoidal and symmetric about the peak. The optical brightness varies between $B \approx 17.5$ and $B \approx 16.7$, although orbit-to-orbit evolution of the overall brightness is apparent. For comparison, in the radio pulsar state the B filter magnitude varies between 18.4 and 17.8 (Thornstensen & Armstrong 2005; Homer et al. 2006).

A wide variety of flaring behavior is also seen, which is associated with the accretion disk state. Some of these flares are very rapid, lasting less than 1 minute, with a rise time that is unresolved at our 10 s (OM) and 13 s (MDM) cadences. A good example of this phenomenon can be seen in the MDM light curve on December 26.51 UT. At the other extreme is a continuous episode of strong flaring on December 28 that lasts 3.6 hr, or 3/4 of the binary orbit. Low-level flaring is present almost continuously for the entire 2013 November *XMM-Newton* observation and the MDM 2013 January 3 observation. We do not see any optical moding behavior that resembles the X-ray variability. In all cases, the optical variability can be characterized as positive flares superposed on the otherwise smooth heating light curve.

The B filter photometric data obtained with the *XMM-Newton* OM further reveal that the brightest optical flares closely match the prominent X-ray flares. Therefore, the flares in PSR J1023+0038 appear to be broadband phenomena that span from the optical up to at least hard X-rays (as seen with *NuSTAR*; Tendulkar et al. 2014). Of particular note are flares III and XI, which reach peak B filter magnitudes of 15.9 and 15.5, respectively. For some, especially flares I and V, the flux peak occurs at significantly later times than the X-ray one and the optical tail of the flare is much longer (see Figure 4). For the brief but intense X-ray flare labeled as II, there does not appear to be a corresponding optical event, while multiple fainter rapid X-ray flares (with X-ray count rates below 20 s $^{-1}$) seen in Figures 2 and 3 have clear optical counterparts.

To identify any time lags between the X-ray and optical flares, we cross-correlated the *XMM-Newton* X-ray and optical time series binned at 10 s resolution. We first fitted a sine function to the OM observation and subtracted it from the data to remove the orbital modulation. The best-fit sine function results in a period of 4.754 h, consistent with the orbital period of the system. As expected, the cross-correlation between the X-ray and detrended optical data sets reveals a strong correlation, which is dominated by the flares. The time lags among the flares range between -260 s and +160 s, where a positive lag

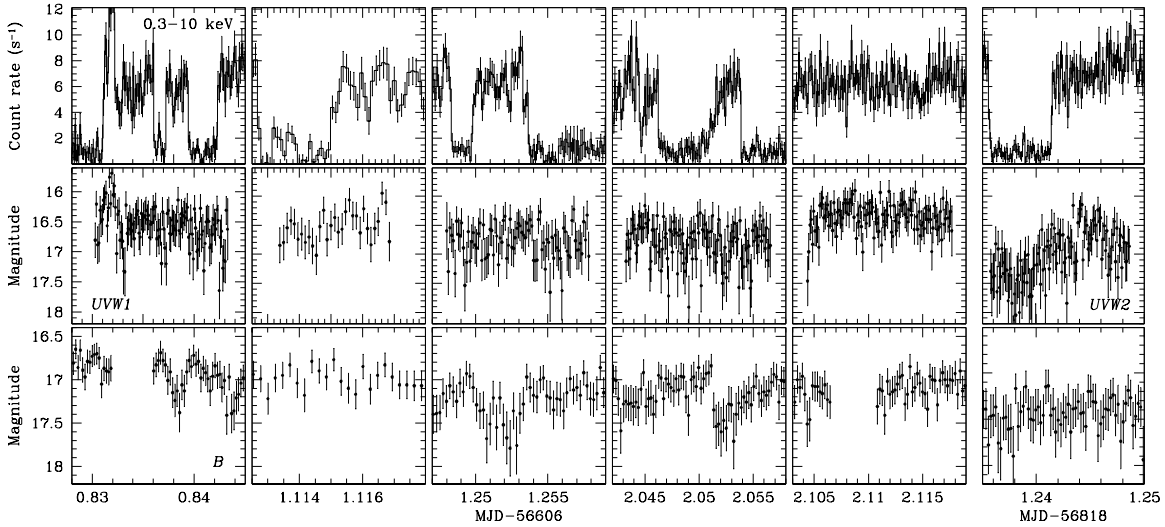


FIG. 12.— Concurrent *XMM-Newton* EPIC X-ray (top), *Swift* UVOT UV (middle), and *XMM-Newton* OM optical (bottom) light curves. All but the right-most set of panels show observations during 2013 November 10-12 when the *Swift* UVW1 was used. The right-most panels show the data during 2014 June 11, when the *Swift* UVOT UVW2 filter was in place.

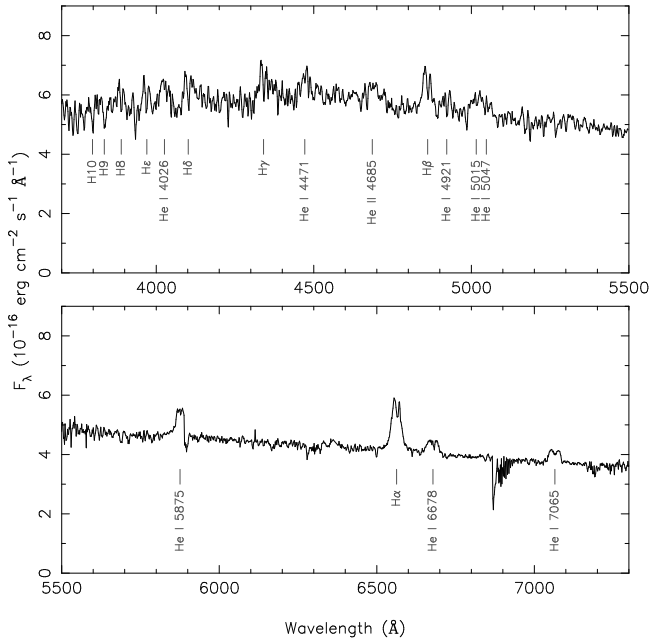


FIG. 13.— VLT X-Shooter spectrum of PSR J1023+0038 from 2013 November 12.

indicates that the X-ray flare precedes the optical one. The strongest correlation is found for the short flares I (with time lag +130 s) in 2013 November and X (with lag 0 s) in 2014 June. For flares III, VIII, IX, and XI the optical leads the X-ray (by -160, -260, -100, -30 s, respectively) although the correlation is weak. The time lags of individual flares are unlikely to be correlated with the orbit due to the variation of the emission site across the orbit with respect to the observer because the compactness of the binary (~ 4 -5 light-s). Indeed, we find no clear trend of the time-lag changes with the orbital phase. Finally, we investigated any correlation of the low level flux variation between the X-ray and optical by removing all significant flares. The resulting correlations

are very weak, consistent with the apparent lack of flux moding in the optical photometric data.

An alternative way to identify low-level optical flux variations correlated with the X-ray mode switching is to consider the optical emission averaged over many low and high X-ray mode intervals. To this end, we first removed the sinusoidal variations of the optical time series. For each X-ray low mode we then computed averaged *B* filter light curves for specific durations (100, 200, and 300 s) and compared them against the high mode immediately before and after using the same duration. The 2013 November data show that the source is on average ~ 0.1 mag brighter during the X-ray low modes relative to the high modes that occur immediately before or after. However, the 2014 June data does not show the same behavior.

The UV emission observed with the *Swift* UVOT (see Figure 12) shows evidence for rapid variability as well. A moderately bright flare that occurs around MJD 56606.83 has an obvious UV counterpart in the *Swift* UVOT data (as seen in the left-most panels of Figure 12). The UVOT UVW1 filter data from 2013 November and the UVW2 filter data from 2014 June cover time periods when multiple low flux intervals are seen in the *XMM-Newton* data. There are no obvious UVW1 brightness variations commensurate with the nearly order of magnitude X-ray flux changes associated with the mode transitions. The 2014 June UVW2 data exhibits a brightness increase that coincides with a low-high X-ray mode transition, although due to the brief UVOT exposure it is not clear if this flux variation occurs consistently for mode transitions.

8. OPTICAL SPECTROSCOPY

In Figure 13, the average of the two individual VLT spectra is plotted. The spectrum is dominated by a blue continuum and strong, double-peaked emission lines of H and He. The spectrum appears similar to other optical spectra of the PSR J1023+0038 binary presented in the literature, both during the active pe-

riod in 2000/2001 (Bond et al. 2002; Wang et al. 2009) and 2013/2014 (Halpern et al. 2013; Takata et al. 2014; Coti Zelati et al. 2014). The optical spectra confirm that the accretion disk was present shortly after the end of the 2013 November X-ray observation. As the optical spectra presented in the literature since the 2013 June transition all show the presence of an accretion disk, it is highly probable that it has been present throughout the 2013 November and 2014 June X-ray observations of PSR J1023+0038. A detailed analysis of these and a series of other spectra acquired since the state transformation of PSR J1023+0038 will be presented in a subsequent paper.

9. RADIO PULSATION SEARCH

As reported in Stappers et al. (2014), the 2013 June reappearance of the accretion disk in PSR J1023+0038 was accompanied by cessation of its bright radio pulsations. To verify this using the 2013 November and 2014 June observations, the radio data were all folded with the ephemeris derived prior to the pulsar disappearance in 2013 June. In both cases sub-integration times of 10 s were used with 1600 frequency channels of with 0.25 MHz for the LT and 512 frequency channels of width 0.3125 MHz for the WSRT data. No radio pulsations were detected around the pulsar period.

Conceivably, if the rotation-powered pulsar emission mechanism is actually still active, the radio pulsations may be highly intermittent such that they may only be present in one of the three distinct X-ray flux modes. In such a scenario, the radio emission is either quenched or severely obscured in the other modes and is only able to “break through” during one mode. To investigate this possibility, we divided the radio observations into time segments that match the times of the high, low, and flare modes observed during the simultaneous *XMM-Newton* observations. For this purpose, we defined an X-ray low mode when the count rate is less than 3 counts s^{-1} and the duration of the low mode is more than 40 s. This resulted in 70 and 35 low mode intervals overlapping with the LT and the WSRT data, respectively. The data in these sections were then corrected for the new, local ephemerides derived from the X-ray data (from Archibald et al. 2014) and subsequently a search in period and dispersion measure (DM) was undertaken for each section. The period search range was 0.01 μs and the DM search range was 3 $\text{cm}^{-3} \text{pc}$. These values were chosen to allow for significant changes in the orbital parameters and/or in the electron column along the line of sight due to material being lost from the companion, or due to the accretion disk. To a signal-to-noise limit of 6 we find no evidence of pulsed emission during any of the low mode intervals in either the LT or WSRT data. We note that these data span a wide range of orbital phases when the pulsar has previously been detected with signal-to-noise ratios of many tens in similar integration times. We performed the same analysis on flares that occur during the radio observation with no significant detection of pulsations either. Finally we considered a long sequence of high mode X-ray emission (MJD 56607.348–56607.385) overlapping with the LT data and also find no significant pulsed signal.

10. RADIO IMAGING

The two-hour long VLA observation made at 5 and 7 GHz at the beginning of the 2013 November campaign shows a strong detection, with a flat spectrum ($\alpha = 0.09 \pm 0.18$, where flux density is proportional to ν^α) and flux density which varies rapidly between 60 and 280 μJy (see left panel of Figure 14). In the 5 GHz e-EVN VLBI observations made shortly after the 2013 November observations we obtain a marginal detection (3.8σ peak with flux density 50 μJy at the precise position of the pulsar predicted by the astrometric solution of Deller et al. 2012); the much sparser *uv* coverage and the faintness of the source precluded any detection of variability on a sub-observation timescale. In the shorter 2–4 GHz VLA observation made 20 hours later, the source is not detected in the combined dataset, with a 3σ upper limit of 30 μJy . When a lightcurve is made with a resolution of 4 minutes, two tentative, 3σ detections with peak flux density $\sim 60 \mu\text{Jy}$ are made (right panel of Figure 14). Finally, PSR J1023+0038 is not detected in the 140 MHz LOFAR observations, although the upper limit of several mJy is not constraining (we note however that, when visible, the pulsar has a period-averaged flux density of $\sim 40 \text{ mJy}$ at 150 MHz; Kondratiev et al., in prep). Deller et al. (2014) show that the variable, flat-spectrum emission seen here persists over many observations made in a six-month period after the November 2013 observations. The observed radio emission is inconsistent with a radio pulsar origin, which should be very steep ($\alpha \sim -2.8$; Archibald et al. 2009) and hence much brighter than the observed emission below 4 GHz, whilst being visible up to $\sim 6 \text{ GHz}$.

Only the last 16 minutes of the VLA data from 2013 November 10 overlap with the *XMM-Newton* EPIC MOS1 exposure¹³. During most of this period the X-ray emission is in the low flux mode, while the radio emission exhibits a rise and fall in flux; the overlap is too brief to establish whether any correlation (potentially with a time lag due to different production sites for the radio and X-ray emission) exists. Although the *XMM-Newton* OM data cover most of the VLA observations, no discernable relation between the radio and optical variability is present. For the 2013 November 11 radio observation, the faintness of the radio emission makes it impossible to identify any relation between the radio and X-ray emission.

Although it is thus difficult to establish whether there is any correlation between the radio and X-ray light curves, we can still examine whether there are any noticeable differences in the radio emission during the different X-ray modes. As discussed in §11.1, this has significant implications for whether the radio pulsar could still be active at any time during the current LMXB state, since the activation of the radio pulsar would lead to the presence of additional steep-spectrum radio emission. A significant portion of the 16 minute overlap between the MOS1 and VLA observations on November 10 is in the low mode, and when we image the VLA data from 18:00:00UT to 18:06:30UT (during this mode) separately, we obtain a flux density of $180 \pm 15 \mu\text{Jy}$ with a spectral index of 0.4 ± 0.6 : consistent with the average value for the whole observation. During the 2–4 GHz observation

¹³ Due to different instrumental overheads, the three EPIC X-ray detectors do not have the same exposure start times.

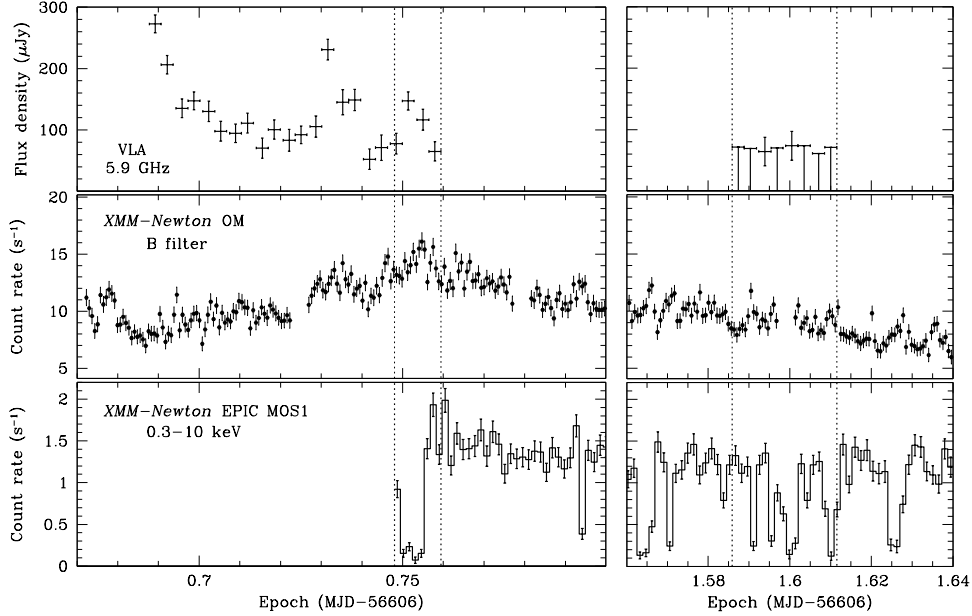


FIG. 14.— Top: VLA 5.9 GHz lightcurves of PSR J1023+0038 from 2013 November 10 and 11. Middle: *XMM-Newton* OM lightcurve. Bottom: *XMM-Newton* EPIC MOS1 lightcurve of PSR J1023+0038. The vertical dotted lines demarcate the time overlap of the radio and X-ray observations.

on 2013 November 11, multiple examples of the low mode are visible, generally for a period of a few minutes at a time. In a radio light curve with 1 minute resolution, no peaks $>2.5\sigma$ ($\sim 100 \mu\text{Jy}$) were visible. In either of these cases (the 6.5 minute low mode image in the November 10 observation and the 1 minute time slices in the November 11 observation) the radio pulsar emission, if unchanged compared to that reported in Archibald et al. (2009), would have been clearly visible. We discuss the implications in §11.1.

11. DISCUSSION

Our unprecedented multi-wavelength campaign of PSR J1023+0038, conducted in 2013 November and 2014 June, shows fascinating phenomenology that provides fresh insight into the properties of PSR J1023+0038 and analogous systems. Based on the wealth of data we have accumulated, we are able to establish the following.

In its LMXB state, PSR J1023+0038 resides in a luminosity range of $L_X \sim 10^{32-34} \text{ erg s}^{-1}$ (0.3–10 keV). The majority of the time is spent at a $3 \times 10^{33} \text{ erg s}^{-1}$ level, during which coherent X-ray pulsations are observed. This implies that active accretion onto the stellar surface takes place (Archibald et al. 2014). During the low flux mode intervals ($\sim 5 \times 10^{32} \text{ erg s}^{-1}$), no pulsed emission is seen, possibly because the accretion flow is unable to reach the star. As shown in Archibald et al. (2014), there is no evidence for pulsations in the low flux mode, with a 95% confidence upper limit on the pulsed fraction of $\sim 2.4\%$. This excludes the possibility that the low mode simply has the same amplitude of pulsations but with scaled-down luminosity. Instead, it appears that the coherent X-ray pulsations are either completely absent or have a comparatively very low amplitude.

The low mode 0.3–10 keV luminosity is ~ 5 times greater than the average luminosity observed in the radio pulsar state in the same energy band ($9 \times 10^{31} \text{ erg}$

s^{-1}). In the radio pulsar state, PSR J1023+0038 showed evidence for broad double-peaked pulsations at the spin period at a 4.5σ with a $\sim 9\%$ pulsed fraction for 0.3–10 keV (Archibald et al. 2010), in addition to the dominant shock emission component. Such pulsations are observed in multiple rotation-powered MSPs and are believed to be produced by heating of the magnetic polar caps by a return flow of relativistic particles from the pulsar magnetosphere. If the X-ray pulsations seen in the radio state are present in the low mode they would appear with a pulsed fraction of $\sim 2\%$, below the upper limit we have derived. Therefore, we cannot rule that the same X-ray pulsations seen in the radio state are present in the low mode of the LMXB state.

Archibald et al. (2014) demonstrated that the pulsations appear to be completely absent during the flares as well. The pulsed fraction upper limit of 1.5% corresponds to a pulsed flux of $0.21 \text{ counts s}^{-1}$, lower than the pulsed flux in the high flux mode ($0.33 \text{ counts s}^{-1}$). This indicates that during the flares the pulsations are strongly suppressed. Therefore, the flares are not simply added flux on top of the high mode emission as the pulsations would still be easily detectable. Instead, the high mode appears to be absent during the flares.

The multiple intense X-ray flares exhibit varied morphologies and temporal behavior. Flaring/burst activity in accreting systems might be from coronal flares arising due to magnetic reconnection events in the accretion disk (e.g., Galeev et al. 1979). Alternatively, an instability in the inner disk may cause a large influx of accreting material towards the compact object (see §11.4). Of particular interest are the long flares interspersed with rapid drops in flux (e.g. III an IX in Figure 4) down to X-ray flux levels comparable to the low mode. This suggests that at least for these flares the emission is not superposed on the high mode flux. Instead, the high mode flux seems to be completely absent and is replaced by the flares.

There is no evidence for the orbital-phase-dependent X-ray modulations that were seen in the radio pulsar state even if all intervals of a single flux mode are folded at the binary period. The non-thermal spectrum in each of the three flux modes is much softer compared to that seen in the radio pulsar state, which had $\Gamma = 1 - 1.2$ (Archibald et al. 2010; Bogdanov et al. 2011). This indicates that the intra-binary shock near the face of the companion, responsible for the X-ray emission in the disk-free state, is absent or completely overwhelmed in the accreting state. The change in the optical heating light curve from an asymmetric to a symmetric, sinusoidal shape favors the absence of this shock emission in the LMXB state. This difference can be explained if the heating by the pulsar wind was asymmetric due to channeling of the pulsar wind by the companion's magnetic field (see, e.g., Li et al. 2014b), while the heating in the LMXB state is by X-rays from the inner disk, which would produce a more symmetric light curve. In addition, if the rotation-powered pulsar mechanism is still active in the LMXB state, the accretion flow may intercept a substantial fraction of the pulsar wind directed towards the companion (see, e.g., Takata et al. 2014).

The sudden drops to a low flux mode appear to be of an entirely different nature than the dips in the X-ray dipper variety of LMXBs (e.g., White & Swank 1982; Smale et al. 1988; Balucinska-Church et al. 2011) as they do not show spectral changes in either soft X-rays (as shown in §6) or hard X-rays (see Tendulkar et al. 2014). In general, based on the results of the X-ray spectral fits presented in §6, any interpretation that evokes obscuration/absorption is unlikely. Since there are negligible spectral changes, especially the value of N_H (see Tables 3 and 4), between the high and low modes, there is no indication for an enhancement in the amount of intervening material during the low mode. There is also no evidence of an X-ray luminosity dependence on the duration and frequency of flares and low flux mode intervals or any correlation between the separation between (and duration of) dips or flares.

Although the extensive data set presented here reveals a wide variety of interesting flaring phenomenology there is evidence that it does not cover the whole range of possible behavior of PSR J1023+0038 in the LMXB state. In particular, in the 100 ks *NuSTAR* observation of PSR J1023+0038 from 2013 October, the system undergoes a prolonged episode of flaring activity that lasts for ~ 10 hours (Tendulkar et al. 2014). For reference, the longest flare in the *XMM-Newton* observations last for ~ 45 minutes and the longest optical flare seen in the MDM data (from 2013 December 28) is ~ 3.6 hours long. It is unclear if this long flare is an exceptionally long and bright flare episode or that it is yet another flux mode.

Based on the multi-wavelength data we have presented here, we can investigate the emission properties of PSR J1023+0038 in its present accreting state spanning the electromagnetic spectrum from the radio to the GeV γ -ray range. Figure 15 shows the spectrum of PSR J1023+0038 across nearly 18 decades of photon frequency. The X-ray spectrum is separated into the three flux modes. In Tendulkar et al. (2014) it was established that the hard X-ray emission observed with *NuSTAR* exhibits the same power-law spectrum and mode switching behavior as the soft X-rays. For reference, here we show

the time-averaged hard X-ray spectrum that is also dominated by the high mode. We also show the *Fermi* LAT flux measurement for PSR J1023+0038 in the LMXB state from Stappers et al. (2014).

As shown in Coti Zelati et al. (2014) and confirmed by our analysis, the optical emission exhibits orbital modulations, which arises due to heating of the face of the secondary star. Sporadic intense flares correlated with the X-ray ones are also seen in both the UV and optical. Neither the UVW1 or B filter photometric light curves exhibit large-amplitude, rapid flux mode switching seen in X-rays.

One important aspect of the observed emission is how the X-ray spectrum in the low, high, and flare modes extrapolates to the UV and optical range. From Figure 15 it is evident that the emission process responsible for the X-ray flux cannot account for the majority of the optical emission as observed with *XMM-Newton* OM (even if we remove the sinusoidal modulations). This provides a plausible explanation for the absence of large-amplitude variations in the B filter data comparable in amplitude to the X-ray mode changes. The extrapolated high mode spectrum in the B filter contributes $\lesssim 10\%$ to the average optical flux. The high mode spectrum can produce $\sim 50\%$ of the observed emission in the *Swift* UVOT UVW2 filter, while in the UVW1 filter the contribution of the high mode declines to $\sim 30\%$. The increase in UVW2 emission that appears to coincide with a low-high mode transition and the lack of comparable brightness variations in the UVW1 band during X-ray mode switches are consistent with these findings.

The extrapolated flare mode spectrum falls well below the flux of the optical flares, suggesting that the X-ray and optical flares are possibly not generated by the same process. Energetically, the peak optical luminosity in the brightest flare ($\sim 1 \times 10^{34}$ erg s $^{-1}$) is well below the peak X-ray luminosity ($\sim 3 \times 10^{34}$ erg s $^{-1}$ for 0.3–10 keV or $\sim 6 \times 10^{34}$ erg s $^{-1}$ for 0.3–79 keV if we take into account the *NuSTAR* data) so it is plausible that reprocessing at a location other than the site of X-ray emission produces the optical flares. However, reprocessing cannot easily account for the puzzling instances where the optical peak precedes the X-ray one. The projected size of the binary is ~ 4 –5 light-seconds so these significant time offsets cannot be attributed to light travel time differences due to emission from different regions of the system. A possible explanation may involve a complex emission spectrum that peaks in both the optical and X-rays.

11.1. Radio Pulsar Enshrouding or Quenching?

It has been suggested (e.g., Takata et al. 2014) that the radio pulsar may be active in the LMXB state. While we believe the detection of X-ray pulsations is evidence that the radio pulsar is quenched in the high mode (but see §11.2), it remains possible that the low and/or flare modes corresponds to times during which the magnetosphere is free of material and the radio pulsar becomes active. Our non-detection of radio pulsations in this mode shows that either the radio pulsar is quenched in the low mode as well, or it is hidden by temporal scattering or absorption. The latter two possibilities can be addressed by our radio imaging observations.

As shown in §10, the continuum radio emission from

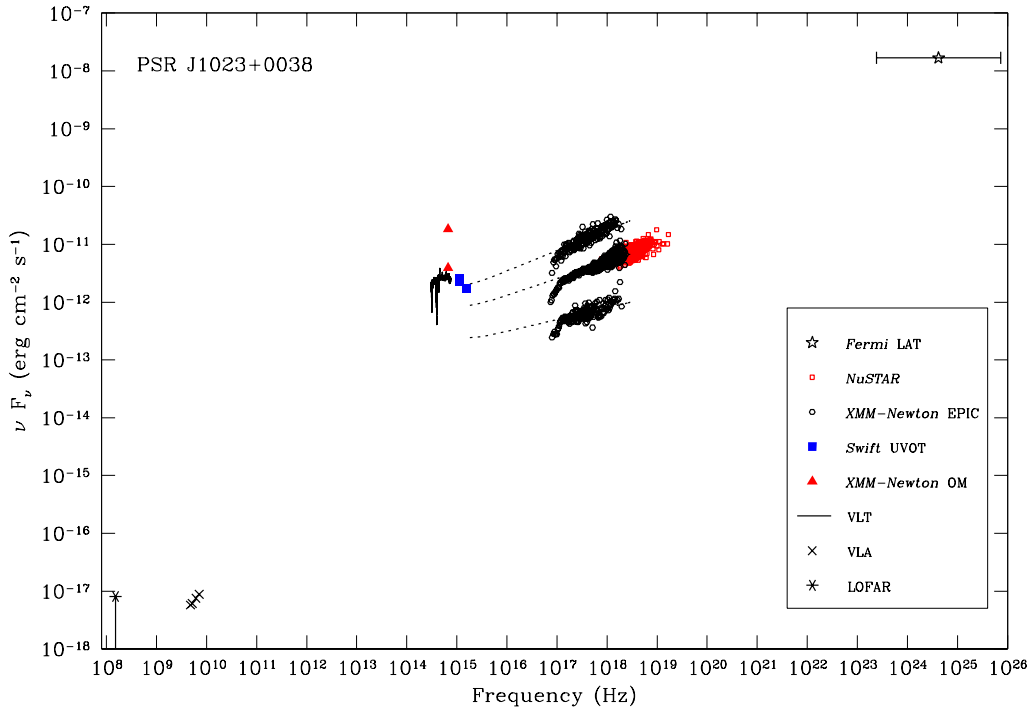


FIG. 15.— The broad-band spectrum of PSR J1023+0038 in the LMXB state spanning from the radio to the γ -ray range. The red triangles show the median and maximum observed fluxes in the B filter as observed with *XMM-Newton* OM, while the blue squares show the mean UV fluxes observed with *Swift* UVOT. The dotted lines show the extrapolation of the best-fit power-law spectra fitted to the flare, high, and low X-ray flux modes observed with *XMM-Newton* EPIC (open circles). The *Fermi* LAT flux in the 1–300 GeV range is based on the value reported in Stappers et al. (2014), while the *NuSTAR* spectrum is taken from Tendulkar et al. (2014).

PSR J1023+0038 is highly variable on timescales of minutes. It also exhibits a spectrum substantially flatter than the radio pulsar spectrum that extends at least up to 18 GHz (Deller et al. 2014). If the radio pulsar was still active but enhanced scattering due to the extra intervening material had obscured the pulsations, the pulsar would still be visible as a steep-spectrum source (potentially with a low frequency turnover due to free-free absorption, as discussed below). There is therefore some other mechanism producing the variable, flat-spectrum continuum emission we see. Neutron stars accreting from a binary companion sometimes exhibit flat-spectrum radio emission, which is assumed to originate from partially self-absorbed synchrotron radiation generated in a collimated, jet-like outflow (e.g., Migliari & Fender 2006; Migliari et al. 2011). The radio continuum behavior we observe is consistent with the jet-powered synchrotron emission seen in other accreting neutron star systems (see Deller et al. 2014, for further details).

This conclusion does not immediately address the possibility of the radio pulsar mechanism operating intermittently during the low or flare modes. However, as noted in §10, the contemporaneous radio and X-ray light curves (14) reveal that there are no obvious changes in either radio flux density or spectral index when comparing the X-ray high mode and low mode time ranges during the 2013 November 10 VLA observation. Likewise, no bright, steep spectrum source appears during the low mode intervals in the 2013 November 11 VLA observation. Therefore, we can immediately rule out scattering alone as a cause of the non-detection of the radio pulsar emission.

The potential impact of free-free absorption is more difficult to exclude. In the radio pulsar state, eclipses due to absorption are seen at frequencies up to several GHz (Archibald et al. 2009, 2013), showing that it is possible even for the relatively tenuous intervening material present in this state to absorb the pulsar signal at low frequencies. In the radio pulsar state the eclipses disappear completely at frequencies of 3 GHz and above, meaning our imaging observations would have easily detected pulsar emission if the absorbing conditions were unchanged in the LMXB state. However, even a modest increase in the density (factor of a few) or length scale (factor of 10) of the absorbing material would increase the free-free optical depth sufficiently to hide any pulsar emission from our radio continuum observations as well as our radio-pulsar-mode observations at frequencies up to ~ 6 GHz. The necessary changes could be driven by, e.g., the increase in heating of the companion, or additional material emanating from the accretion disk.

Exact limits are difficult to place because of the additional dependence on the temperature of the absorbing material, as well as the fact that the spectrum of the pulsar is difficult to measure (the value of -2.8 from Archibald et al. (2009) is particularly steep, even for a millisecond pulsar, and the potential contamination by scintillation means it should be applied here with caution; a shallower radio pulsar spectrum would mean that the radio pulsar emission would still be visible to the VLA up to ~ 10 GHz). In light of these caveats, we cannot categorically rule out an active radio pulsar in the low mode, and we note that a similar scenario — active radio pulsar enshrouded by absorption —

has been proposed for SAX J1808.4–3658 in quiescence (Campana et al. 2004). However, we note that any activation of the radio pulsar in the low mode, even if the radio emission is free-free absorbed, would also have to occur without substantially affecting the ongoing flat-spectrum (jet) emission.

11.2. Pulsar Mode Switching?

An alternative explanation for the observed X-ray pulsations is possible: the pulsar emission mechanism in some cases produces switching between different magnetospheric “modes”, with different radio, X-ray, and γ -ray luminosities and different spin-down rates (Lyne 1971; Hermsen et al. 2013; Allafort et al. 2013). It is therefore possible that PSR J1023+0038 is still active as a radio pulsar but may have entered a different magnetospheric configuration. Since optical observations make it clear that PSR J1023+0038 acquired a disk at about the same time the radio, X-ray, and γ -ray properties changed, Occam’s razor suggests that if PSR J1023+0038 has switched modes it must be linked to the accretion, presumably triggered by the injection of small amounts of hadronic material into the light cylinder, although, to our knowledge, no such mechanism has been proposed.

Energy considerations do not rule out such a scenario: assuming that the spin-down rate has not changed substantially, that would imply that PSR J1023+0038’s X-ray efficiency was 7% (in the high mode, and neglecting any X-ray emission from the disk) and its γ -ray efficiency was 15%; neither number exceeds 100%. The flares can exceed the pulsar’s spin-down luminosity, so presumably these would have to originate in the disk, although this appears to conflict with the fact that the pulsations are suppressed during flares. Accretion-induced mode switching would explain the rapid switching between relatively stable X-ray modes, though as the low mode is still substantially brighter than the radio pulsar’s X-ray emission, we would have to postulate at least two distinct accretion-induced modes.

Accretion-induced mode switching also provides an explanation for the pulsar’s disappearance in radio, although no radio MSP has been observed to null in radio and their broad beaming (in particular PSR J1023+0038’s broad radio profile) makes it unlikely a reconfigured beam could miss the Earth. If the radio pulsar mechanism is active, it should be producing a pulsar wind, and it becomes difficult to see how a disk can remain in the system: the pulsar wind pressure falls off like radiation pressure, but in all disk models, the ram pressure falls off more rapidly so no stable balance can exist outside the light cylinder (Shvartsman 1970), while substantial amounts of material inside the light cylinder would be expected to short out the pulsar mechanism completely.

Overall, we deem accretion-induced mode switching highly unlikely but cannot definitively rule it out. A detection of γ -ray pulsations in the current state would strongly support such an explanation. We are carrying out monitoring campaigns with Arecibo, the Lovell, and the WSRT. These will time the pulsar as soon as it re-activates in radio, which will measure a mean spin-down during the accretion-disk state, possibly ruling out accretion-induced mode switching.

11.3. Comparison with Other Systems

11.3.1. XSS J12270–4859

In 2012 November or December, the peculiar nearby LMXB and bright *Fermi* LAT source XSS J12270–4859 (1RXS J122758.8–485343) underwent a substantial decline in optical/X-ray brightness. Follow-up optical, X-ray, and radio observations revealed that the accretion disk had disappeared and the 1.69 ms radio pulsar has switched on (Bassa et al. 2014; Bogdanov et al. 2014b; Roy et al. 2014). These findings have established that XSS J12270–4859 is a close analog to PSR J1023+0038 and only the third system seen to undergo a MSP to LMXB (or vice-versa) state transformation.

In its LMXB state, XSS J12270–4859 exhibited a rapid variability pattern similar to what we observe in PSR J1023+0038 (Saitou et al. 2009; de Martino et al. 2010, 2013). Specifically, the same rapid switches between two flux modes and occasional intense flares are seen. This implies that in the LMXB state the same processes operate in both systems, which was recently confirmed with the detection of X-ray pulsations in the high mode of this object (Papitto et al. 2014b).

The drops to the low mode had ingress and egress timescales of ~ 10 s and low mode durations between 200 and 800 s. These transitions were observed in the X-ray and near-UV bands but were absent in the ground-based optical observations, suggesting an origin close to the neutron star. de Martino et al. (2010) noted that the dips occurring immediately after flares were attributed to a rapid episode of accretion onto the neutron star (corresponding to the flare) and the corresponding emptying of a reservoir of accreting material (the dip) and subsequent filling up of the inner regions of the accretion disk. In contrast, in the long X-ray exposures of PSR J1023+0038 presented here, we do not find preceding flares for all the dips.

11.3.2. PSR J1824–2452I

The X-ray transient IGR J18245–2452 in M28 contains the first NS observed to switch between rotation-powered and accretion-powered pulsations (Papitto et al. 2013). The source exhibited a luminous X-ray outburst in March 2013 reaching a peak 0.5–10 keV outburst luminosity of $\sim 5 \times 10^{36}$ erg s $^{-1}$ (based on *Swift* XRT spectra; Linares et al. 2014). Papitto et al. (2013) discovered 254 Hz X-ray pulsations during two *XMM-Newton* observations taken on 2013 April 3 and 13. Remarkably, the spin frequency was identical to that of a previously known radio MSP, PSR J1824–2452I. The system was detected again as a radio MSP after the 2013 outburst.

In an archival 200-ks *Chandra* ACIS-S observation of PSR J1824–2452I in 2008 August (Papitto et al. 2013; Linares et al. 2014) the system was at a luminosity level of $\sim 10^{33}$ erg s $^{-1}$ and also exhibited large-amplitude variability. While no strong flares were observed, one low flux mode flux interval lasted for nearly 10 hours instead of several minutes like in PSR J1023+0038. The transitions between the two flux states in PSR J1824–2452I occurred on time-scales of ~ 500 s instead of ~ 10 s. The reason for these substantial differences is not known but probably depends on the particular combination of pulsar and binary parameters and the accretion rate.

11.3.3. *SAX J1808.4-3658*

The transient X-ray source SAX J1808.4-3658 is the first accreting neutron star binary from which coherent millisecond X-ray pulsations were detected (Wijnands & van der Klis 1998). In its quiescent state, Campana et al. (2002) and Heinke et al. (2009) have found 0.5-10 keV luminosities of $(8-9) \times 10^{31} \text{ erg s}^{-1}$ assuming a distance of 3.5 kpc. At this level SAX J1808.4-3658 exhibits an X-ray spectrum that is well-fitted by an absorbed power-law ($\Gamma \approx 1.7-1.8$) with no requirement for a thermal component.

During the return from the 2005 outburst state to quiescence, long-term *Swift* monitoring revealed that SAX J1808.4-3658 alternated between two different luminosity levels, $\approx 1 \times 10^{33}$ and $\approx 3 \times 10^{32} \text{ erg s}^{-1}$ (for $D = 3.5 \text{ kpc}$), in observations separated by \sim days (Campana et al. 2008). These luminosity levels are comparable to the high and low modes seen in PSR J1023+0038, XSS J12270-4859, and J1824-2452I, suggesting that SAX J1808.4-3658 possibly experienced the same moding behavior during this period (although due to the limited photon statistics this cannot be firmly verified). If we further extend the analogy with these systems, the true quiescent level of SAX J1808.4-3658 at $\lesssim 10^{32} \text{ erg s}^{-1}$ possibly corresponds to the disk-free radio pulsar state (Homer et al. 2001) in which an intra-binary shock dominates the X-ray emission, as found PSR J1023+0038 and analogous systems (see Archibald et al. 2010; Bogdanov et al. 2005, 2011, 2014a).

11.3.4. *Centaurus X-4*

Recently, Chakrabarty et al. (2014) conducted joint *NuSTAR* and *XMM-Newton* observations of the long-known, nearby LMXB Cen X-4. Although at a comparable luminosity level, unlike PSR J1023+0038, the non-thermal component of Cen X-4 in quiescence shows a spectral cutoff at $\sim 10 \text{ keV}$. As shown in Tendulkar et al. (2014), for PSR J1023+0038, the non-thermal emission is present at least up to $\sim 30 \text{ keV}$. This implies that the non-thermal component in the spectrum of Cen X-4 may be of an entirely different origin than what is seen in PSR J1023+0038. In addition, Cen X-4 exhibits a dominant thermal emission component, presumably due to radiation from most of the neutron star surface. In contrast, PSR J1023+0038 does not show a prominent thermal component, an indication that the accretion flow does not induce substantial heating of the neutron star. The possible presence of a faint thermal component in the high flux mode of PSR J1023+0038 indicates that the polar caps are heated only superficially and the deposited heat is quickly reradiated.

The marked differences in observed properties between the two systems might be ascribed to a very weakly magnetized compact object in Cen X-4, such that the accretion flow can proceed unimpeded down to the NS surface (see, e.g., D’Angelo et al. 2014, for further details).

11.4. *Previous Interpretations*

Prior to results from Archibald et al. (2014) and from the analysis presented here, although the presence of an accretion disk was undisputed, it was unclear whether the pulsar wind in the PSR J1023+0038 binary was still active or if material was actually flowing down to the

neutron star surface, even intermittently. Several interpretations have been offered to account for the observed behavior.

Linares et al. (2014) proposed that this bi-stable X-ray flux switching in PSR J1824-2452I is due to rapid transitions between magnetospheric accretion (high mode) and pulsar wind shock emission (low mode) regimes, with the two different non-thermal emission mechanisms coincidentally producing the same power-law spectrum with $\Gamma \approx 1.7$.

An alternative interpretation was offered by Papitto et al. (2014a) to account for the properties of XSS J12270-4859 in its LMXB state, which is fully applicable to PSR J1023+0038 as well. The mode switches were attributed to rapid emptying and refilling of the inner accretion disk due to the action of the pulsar wind or the propeller mechanism, with little to no accretion taking place.

Stappers et al. (2014), Takata et al. (2014), and Coti Zelati et al. (2014) have provided yet another explanation for the multi-wavelength phenomenology of PSR J1023+0038. In their model, the pulsar wind is still active but the radio pulsations are dispersed by evaporating material from the accretion disk or material that is engulfing the pulsar. The great increase in X-ray luminosity during the accreting state compared to the radio pulsar state is then the result of a stronger intra-binary shock since the pulsar wind encounters a stronger outflow from the companion that is much closer to the pulsar. The enhancement in γ -ray emission can be accounted for by inverse Compton scattering of UV emission by particles from the pulsar wind.

Based on the wealth of observational information we have presented here, we can evaluate the viability of the interpretations described above. Any self-consistent explanation for the behavior of PSR J1023+0038, and by extension quite likely XSS J12270-4859 and PSR J1824-2452I as well, needs to account for the large-amplitude X-ray variability, especially the intermittent, rapid ($\sim 10 \text{ sec}$) switching between two discrete flux levels, the coherent X-ray pulsations during the high flux mode, and the flat-spectrum radio emission. The interpretations that invoke an active pulsar wind during the high flux mode in particular are difficult to reconcile with the observed X-ray pulsations and flat radio spectrum, which leaves accretion processes as the more probable explanation for this emission.

11.5. *The Accretion Physics of PSR J1023+0038*

X-ray binaries containing neutron stars are routinely studied in great detail when actively accreting ($\gtrsim 10^{35} \text{ erg s}^{-1}$) and most of our understanding of the physics of accretion onto magnetized neutron stars comes from such instances. Specifically, it is well-established that at high luminosities matter flows down to the neutron star surface, as evidenced by the detection of thermonuclear bursts in LMXBs and X-ray pulsations in accreting millisecond X-ray pulsars (AMXPs; see, e.g., Patruno & Watts 2012, and references therein). However, none of the known AMXPs are close enough to Earth to easily establish whether channeled accretion also reaches the neutron star during quiescence. The discovery of coherent X-ray pulsations from PSR J1023+0038 at a luminosity level of $\sim 10^{33} \text{ erg s}^{-1}$ pro-

vides crucial information regarding the physical processes that operate in quiescence.

In basic accretion models onto magnetized stars, the accretion disk has a truncation at the magnetospheric radius, where the ram pressure of the infalling material balances the magnetic pressure of the field (Pringle & Rees 1972). This occurs at a distance $r_m \simeq (BR^3)^{4/7} (GM/2)^{1/7} \dot{M}^{-2/7}$. If this magnetospheric radius exceeds the co-rotation radius, $r_c = GM/\Omega^2$, where the Keplerian orbital velocity of the accretion flow equals the rotation rate of the neutron star, the system enters the “propeller” regime (Illarionov & Sunyaev 1975). The resulting centrifugal barrier created by the rapidly-spinning neutron star does not permit accretion and expels the infalling material from the system. For low enough mass inflow rates, the radio pulsar mechanism might also activate and sweep the inflowing matter away. Based on this, such models predict that accretion onto the neutron star surface is an unlikely mechanism for producing the quiescent emission of AMXPs, as it requires very low magnetic fields and/or long spin periods. However, our findings for PSR J1023+0038 suggest that accretion onto the neutron star surface does occur despite the remarkably low implied accretion rate and rapid spin of the star, which is also sufficiently magnetized to force channeled accretion.

If the X-ray luminosity observed in the high flux mode is generated entirely due to the liberation of gravitational potential energy of the material landing on the stellar surface, the implied rate is $\sim 9 \times 10^{-13} M_\odot \text{ yr}^{-1}$, corresponding to just $\sim 10^{-5} - 10^{-4} L_{\text{Edd}}$. It remains unclear, however, what portion of the gas flowing through the disk actually reaches the star so this value provides a lower limit on the accretion rate at $\sim r_c$.

For the classical thin disk model, even if the majority of inflowing gas is expelled when it reaches $\sim r_c$, it should still generate a high X-ray luminosity, which is not observed in PSR J1023+0038. However, it is important to note that the relatively low X-ray luminosity of PSR J1023+0038 corresponds to a low accretion rate onto the magnetosphere only if the accretion disk is radiatively efficient. In the case of an intrinsically radiatively inefficient flow (Rees et al. 1982), the disk changes from being optically thick to being optically thin but geometrically thick. However, even in this scenario, the bulk of the material would eventually accrete onto the neutron star, producing a large X-ray luminosity in the process, which is at odds with the low luminosities seen in quiescent LMXBs. To circumvent this problem, it has been proposed that most of the material is driven out (e.g., by the propeller mechanism) and its gravitational potential energy is not emitted as radiation. A sufficiently high accretion rate can result in $r_m \approx r_c$ such that a small fraction of the material can reach the stellar surface. In this interpretation, some mechanism still needs to account for the intermittent but very steady episodes of accretion (corresponding to the high flux mode).

One possibility is the so-called “trapped” disk (Spruit & Taam 1993), where gas is accumulated (trapped) near co-rotation, which exerts inward pressure to balance the magnetic stress (see, e.g., D’Angelo & Spruit 2010, 2012). In this scenario, the switching between the high and low modes can be in-

terpreted as being due to the rapid emptying and refilling of this reservoir of trapped material. Although the cyclic variation between high and low accretion rate is a feature of the trapped disk model, the manner in which this occurs is not consistent with the square-wave-like X-ray mode switching observed in PSR J1023+0038, especially the remarkably steady luminosity levels in both the high and low modes. The oscillation timescales are much shorter (up to ~ 100 – 1000 s) than the variability observed in PSR J1023+0038. In addition, flare-like spikes in accretion rate occur – the disk goes through cycles of building up gas and then dumping it onto the star, so generally the building up timescales are longer than the dumping timescales.

Throughout the discussion above, it is assumed that the gas can effectively couple to the magnetic field. However, the magnetic field can become disconnected from the gas because of field line twisting (Lovelace et al. 1995), at which point it is not completely clear how the gas latches onto the field lines to accrete onto the star. If there is perfect coupling, in the propeller regime no matter is able to accrete for low accretion. However, simulations (which are ideal MHD with numerical diffusion) show that some accretion through the centrifugal barrier can occur because the gas is disconnected from the fast-spinning magnetosphere (see, e.g., Romanova et al 2004; Lii et al. 2014). In D’Angelo et al. (2014), the results of these simulations were applied to this modified propeller – most of the gas is expelled but a small fraction is accreted, and this fraction could, in principle, produce coherent X-ray pulsations.

A qualitative description for the moding behavior might involve a transition between the trapped disk and propeller mode. A disk may remain trapped because of extra gas in the inner region of the disk (compared with a normal accretion disk), which absorbs the angular momentum from the disk-field interaction. This state could co-exist with an outflow of gas, which could then erode enough gas in the disk so that the system enters the propeller regime, and no gas accretes onto the star, hence it becomes much dimmer. The reverse could occur as well. If not all the material around r_m is expelled in an outflow, gas begins to build up into a trapped disk again. Given sufficient build up of matter, accretion on to the star can commence again, which will result in a rapid jump in luminosity. However, detailed modeling is necessary to assess the viability of this hybrid trapped disk – propeller mode scenario.

One of the most notable features of the high X-ray flux mode in PSR J1023+0038 is that, despite its intermittent nature, the luminosity and pulse shape are highly reproducible and stable on time scales up to at least seven months (corresponding to the separation between the two *XMM-Newton* observations). In addition, the duty cycle of the high mode is $\sim 70\%$, meaning that this steady accretion occurs most of the time. Any accretion model that requires an instability to instigate accretion onto the neutron star would thus have difficulties explaining this steady behavior because the instability would result in brief episodes of accretion and much more erratic burst-like flux variability.

In this sense, the occasional flares observed in our X-ray data are more consistent with being due to accretion flow instabilities. For instance, Kulkarni & Romanova

(2008) have found that Rayleigh-Taylor instabilities may produce “tongues” of plasma that break through the magnetosphere and reach the stellar surface close to the equator. The shape and number of the tongues changes with time on the inner disc dynamical timescale. The shape, number and location of the resulting hot spots varies on timescales comparable to the dynamical time scale of the inner disk. This erratic behavior can, in principle, account for the absence of coherent X-ray pulsations during the flare mode of PSR J1023+0038. However, the instability appears for cases when the angles between the spin and magnetic axes are $\theta \lesssim 30^\circ$. The double-peaked X-ray pulse profiles of PSR J1023+0038 suggests a greater misalignment of the two axes for this neutron star. In addition, as per Kulkarni & Romanova (2008), for neutron stars such instabilities occur for accretion rates above $\dot{M}_{*,\text{crit}} \approx 2.2 \times 10^{-9} \text{M}_\odot \text{yr}^{-1} (B/10^9 \text{G})^2 (R_{NS}/10 \text{km})^{5/2} (M_{NS}/1.4 \text{M}_\odot)^{-1/2}$. For the magnetic field strength of $9.7 \times 10^7 \text{G}$ deduced from radio timing (Archibald et al. 2013), $M_{NS} = 1.4 \text{M}_\odot$, and $R_{NS} = 10 \text{km}$, for PSR J1023+0038 we obtain $\dot{M}_{*,\text{crit}} \approx 2 \times 10^{-11} \text{M}_\odot \text{yr}^{-1}$, an order of magnitude greater than implied by the flare luminosity. Finally, the timescales for the instability are much shorter than the variability we observe in PSR J1023+0038; they are typically of order a few times the spin period instead of tens of seconds. In light of these differences, although the basic phenomenology seems to fit pretty well, especially the absence of pulsations in the flare mode, it is not clear whether this instability model is applicable to the flare mode of PSR J1023+0038.

It is apparent that further theoretical efforts are required to establish which, if any, existing models of accretion can adequately explain the observed behavior of PSR J1023+0038. Specifically, it is necessary to consider a process that ejects the bulk of the accretion flow material while maintaining “quiescent” level X-ray luminosities. The remaining material needs to be able to reach the neutron star polar caps via a steady channelled flow that is restricted to a very narrow range of accretion rates. This flow undergoes occasional interruptions, manifested by abrupt changes to a similarly stable but lower luminosity mode. This pattern is interspersed with short-lived episodes of higher X-ray luminosity, presumably due to unstable accretion.

12. CONCLUSIONS

We have presented extensive multi-wavelength observations of PSR J1023+0038 in its LMXB state. The wealth of data offer unique insight into the behavior of accreting MSPs in the quiescent regime. The system appears to exhibit short-lived but very frequent and exceptionally stable episodes of channelled accretion onto the stellar magnetic poles. This activity appears to be limited to a remarkably narrow luminosity range around $\sim 3 \times 10^{33} \text{erg s}^{-1}$. The frequent and rapid switches to a second, lower luminosity mode with $\sim 5 \times 10^{32} \text{erg s}^{-1}$ during which no pulsations are observed, can be interpreted as being non-accreting intervals. At least a por-

tion of the occasional X-ray/optical flares may be produced by enhanced, spasmodic accretion due to some form of disk instability or deformation of the magnetosphere. Although certain propeller and trapped disk models predict qualitatively similar behavior, none are fully consistent with the observed properties of PSR J1023+0038, especially the accretion-induced pulsations produced at a luminosity ~ 100 times lower than previously observed in an AMXP.

The episodic reappearance of an accretion disk in PSR J1023+0038 implies that the current disk will eventually recede and the binary will revert to its radio pulsar state yet again. In such an event, it is important to identify any differences in the system between the pre and post LMXB state periods.

Further insight into this peculiar system can be gained with additional observations, especially contemporaneous X-ray and continuum radio observations over a long time span, to conclusively establish any correlated variability between the two bands. Perhaps most importantly, it is crucial to monitor the long-term spin behavior of PSR J1023+0038 in order to establish what kinds of torques are being imparted onto the neutron star, which may have profound implications for understanding of accretion onto highly magnetized objects, in general.

A.M.A. and J.W.T.H. acknowledge support from a Vrije Competitie grant from NWO. A.T.D. acknowledges support from an NWO Veni Fellowship. J.W.T.H. and A.P. acknowledge support from NWO Vidi grants. J.W.T.H. also acknowledges funding from an ERC Starting Grant “DRAGNET” (337062). A portion of the results presented was based on observations obtained with *XMM-Newton*, an ESA science mission with instruments and contributions directly funded by ESA Member States and NASA. This work was based in part on observations obtained at the MDM Observatory, operated by Dartmouth College, Columbia University, Ohio State University, Ohio University, and the University of Michigan. This research is based in part on observations made with ESO Telescopes at the Paranal Observatory under programme ID 292-5011. The WSRT is operated by ASTRON (Netherlands Institute for Radio Astronomy) with support from the Netherlands Foundation for Scientific Research. Access to the Lovell Telescope is supported through an STFC consolidated grant. The National Radio Astronomy Observatory is a facility of the National Science Foundation operated under cooperative agreement by Associated Universities, Inc. The EVN (<http://www.evlbi.org>) is a joint facility of European, Chinese, South African, and other radio astronomy institutes funded by their national research councils. LOFAR, the Low Frequency Array designed and constructed by ASTRON, has facilities in several countries, that are owned by various parties (each with their own funding sources), and that are collectively operated by the International LOFAR Telescope (ILT) foundation under a joint scientific policy. This research has made use of the NASA Astrophysics Data System (ADS).

Facilities: *XMM*, *Swift*, *ESO/VLT*

REFERENCES

- Allafort, A., Baldini, L., Ballet, J., et al. 2013, *ApJ*, 777, L2
 Alpar, M. A., Cheng, A. F., M. A. Ruderman, M. A., & Shaham, J. 1982, *Nature*, 300, 728

- Archibald, A. M., Bogdanov, S., Patruno, A., et al. 2014, *ApJ*, submitted (eprint arXiv:1412.1306)
- Archibald, A. M., Kaspi, V. M., Bogdanov, S., Hessels, J. W. T., Stairs, I. H., Ransom, S. M., McLaughlin, M. A., & Lorimer, D. 2010, *ApJ*, 722, 88
- Archibald, A. M., Kaspi, V. M., Hessels, J. W. T., et al. 2014, *ApJ*, submitted (eprint arXiv:1311.5161)
- Archibald, A. M., Stairs, I. H., Ransom, S. M., et al. 2009, *Science*, 324, 1411
- Arnaud, K. A. 1996, *ASPC*, 101, 17
- Balucinska-Church, M., Schulz, N. S., Wilms, J., Gibiec, A., Hanke, M., Spencer, R. E., Rushton, A., Church, M. J. 2011, *A&A*, 530, 102
- Bassa, C. G., Patruno, A., Hessels, J. W. T., Keane, E. F., Monard, B., Mahony, E. K., Archibald, A. M., Bogdanov, S., Janssen, G. H., Stappers, B. W., Tendulkar, S. 2014, *MNRAS*, 441, 1825
- Bogdanov, S., Grindlay, J. E., & van den Berg, M. 2005, *ApJ*, 630, 1029
- Bogdanov, S., Archibald, A. M., Hessels, J. W. T., Kaspi, V. M., Lorimer, D., McLaughlin, M. A., Ransom, S. M., Stairs, I. H. 2011a, *ApJ*, 742, 97
- Bogdanov, S. 2013, *ApJ*, 762, 96
- Bogdanov, S., Esposito, P., Crawford, F., Possenti, A., McLaughlin, M. A., Freire, P. 2014a, *ApJ*, 781, 6
- Bogdanov, S., Patruno, A., Archibald, A. M., Bassa, C., Hessels, J. W. T., Janssen, G. H., & Stappers, B. W. 2014b, *ApJ*, 789, 40
- Bond, H. E., White, R. L., Becker, R. H., & O'Brien, M. S. 2002, *ApJ*, 114, 1359
- Campana, S., Colpi, M., Mereghetti, S., Stella, L., & Tavani, M. 1998, *A&ARv*, 8, 279
- Campana, S., D'Avanzo, P., Casares, J., Covino, S., Israel, G., Marconi, G., Hynes, R., Charles, P., Stella, L. 2004, *ApJ*, 614, L49
- Campana, S., Stella, L., Gastaldello, F., Mereghetti, S., Colpi, M., Israel, G. L., Burderi, L., Di Salvo, T., Robba, R. N. 2002, *ApJ*, 575, L15
- Campana, S., Stella, L., & Kennea, J. A. 2008, *ApJ*, 648, L99
- Cavaliere, A., & Fusco-Femiano, R. 1976, *A&A*, 49, 137
- Chakrabarty, D., Tomsick, J. A., Grefenstette, B. W., et al. 2014, *ApJ*, 797, 92
- Cohen, A. S., Lane, W. M., Cotton, W. D., et al. 2007, *AJ*, 134, 1245
- Corbel, S., Kaaret, P., Fender, R. P., Tzioumis, A. K., Tomsick, J. A., Orosz, J. A. 2005, *ApJ*, 632, 504
- Coti Zelati, F., Baglio, M. C., Campana, S., et al. 2014, *MNRAS*, 444, 1783
- D'Angelo, C. R., & H. C. Spruit H. C. 2010, *MNRAS*, 406, 1208
- D'Angelo, C. R., & H. C. Spruit H. 2012, *MNRAS*, 420, 416
- D'Angelo, C. R., Fridriksson, J. K., Messenger, C., A. Patruno, A. 2014, submitted (ArXiv e-prints 1410.3760)
- Davis, J. E. 2001, *ApJ*, 562, 575
- Deller, A. T., Archibald, A. M., Briskin, W. F., Chatterjee, S., Janssen, G. H., Kaspi, V. M., Lorimer, D., Lyne, A. G., McLaughlin, M. A., Ransom, S., Stairs, I. H., & Stappers, B. 2012, *ApJ*, 756, L25
- Deller, A. T., Moldón, J., Miller-Jones, J. C. A., et al. 2014, *ApJ*, submitted (eprint arXiv:1412.5155)
- de Martino, D., Belloni, T., Falanga, M., Papitto, A., Motta, S., Pellizzoni, A., Evangelista, Y., Piano, G., Masetti, N., Bonnet-Bidaud, J.-M., Mouchet, M., Mukai, K., Possenti, A. 2013, *A&A*, 550, 89
- de Martino, D., Falanga, M., Bonnet-Bidaud, J.-M., Belloni, T., Mouchet, M., Masetti, N., Andruchow, I., Cellone, S. A., Mukai, K., Matt, G. 2010, *A&A*, 515, 25
- Galeev, A. A., Rosner, R., & Vaiana, G. S. 1979, *ApJ*, 229, 318
- Halpern, J. P., Gaidos, E., Sheffield, A., Price-Whelan, A. M., & Bogdanov, S. 2013, *The Astronomer's Telegram*, 5514, 1
- Heinke, C. O., Jonker, P. G., Wijnands, R., Deloye, C. J., Taam, R. E. 2009, *ApJ*, 691, 1035
- Hermesen, W., Hessels, J. W. T., Kuiper, L., et al. 2013, *Science*, 339, 436
- Homer, L., Charles, P. A., Chakrabarty, D., & van Zyl, L. 2001, *MNRAS*, 325, 1471
- Homer, L., Szkody, P., Chen, B., et al. 2006, *AJ*, 131, 562
- Illarionov, A. F., & Sunyaev, R. A. 1975, *A&A*, 39, 185
- Kulkarni, A. K., & Romanova, M. M. 2008, *MNRAS*, 386, 673
- Li, K. L., Kong, A. K. H., Takata, J., Cheng, K. S., Tam, P. H. T., Hui, C. Y., Jin, R. 2014, *ApJ*, in press (eprint arXiv:1410.4563)
- Li, M., Halpern, J. P., Thorstensen, J. R. 2014, *ApJ*, 795, 115
- Liil4, P. S., Romanova, M. M., Ustyugova, G. V., Koldoba, A. V., Lovelace, R. V. E. 2014, *MNRAS*, 441, 86
- Linares, M., Bahramian, A., Heinke, C., Wijnands, R., Patruno, A., Altamirano, D., Homan, J., Bogdanov, S., Pooley, D. 2014, *MNRAS*, 438, 251
- Linares, M. 2014, *ApJ*, 795, 72
- Lovelace, R. V. E., Romanova, M. M., Bisnovatyi-Kogan, G. S. 1995, *MNRAS*, 275, 244
- Lyne, A. G. 1971, *MNRAS*, 153, 27
- Mason, K. O., Breeveld, A., Much, R., et al. 2001, *A&A*, 365, L36
- Migliari, S., & Fender, R. P. 2006, *MNRAS*, 366, 79
- Migliari, S., Miller-Jones, J. C. A., & Russell, D. M. 2011, *MNRAS*, 415, 2407
- Papitto, A., Ferrigno, C., Bozzo, E., et al. 2013, *Nature*, 501, 517
- Papitto, A., Torres, D. F., Li, J. 2014a, *MNRAS*, 438, 2105
- Papitto, A., et al. 2014, *MNRAS*, submitted (eprint arXiv:1412.4252)
- Patruno, A., Archibald, A. M., Hessels, J. W. T., Bogdanov, S., Stappers, B. W., Bassa, C. G., Janssen, G. H., Kaspi, V. M., Tendulkar, S., Lyne, A. G. 2014, *ApJ*, 781, L3
- Patruno, A., & Watts, A. L. to appear in "Timing neutron stars: pulsations, oscillations and explosions", T. Belloni, M. Mendez, C. M. Zhang Eds., *ASSL*, Springer
- Pringle, J. E., & Rees, M. J. 1972, *A&A*, 21, 1
- Rees, M. J., Begelman, M. C., Blandford, R. D., & Phinney, E. S., 1982, *Nature*, 295, 17
- Romanova, M. M., Ustyugova, G. V., Koldoba, A. V., Lovelace, R. V. E. 2004, *ApJ*, 616, L151
- Roy, J., Bhattacharyya, B., Ray, P. S. 2014, *The Astronomer's Telegram*, 5890, 1
- Saitou, K., Tsujimoto, M., Ebisawa, K., & Ishida, M. 2009, *PASJ*, 61, L13
- Smale, A. P., Mason, K. O., White, N. E., Gottwald, M. 1988, *MNRAS*, 232, 647
- Spruit, H. C., & Taam, R. E. 1993, *ApJ*, 402, 593
- Shvartsman, V. F. 1970, *AZh*, 47, 660
- Stappers, B. W., Archibald, A. M., Hessels, J. W. T., Bassa, C. G., Bogdanov, S., Janssen, G. H., Kaspi, V. M., Lyne, A. G., Patruno, A., Tendulkar, S., Hill, A. B., Glanzman, T. 2014, *ApJ*, 790, 39
- Strüder, L. et al. 2001, *A&A*, 365, L18
- Szkody, P., et al. 2003, *ApJ*, 126, 1499
- Tam, P. H. T., Hui, C. Y., Huang, R. H. H., Kong, A. K. H., Takata, J., Lin, L. C. C., Yang, Y. J., Cheng, K. S., & Taam, R. E. 2010, *ApJ*, 724, 207
- Takata, J., Li, K. L., Leung, G. C. K., Kong, A. K. H., Tam, P. H. T., Hui, C. Y., Wu, E. M. H., Xing, Y., Cao, Y., Tang, S., Wang, Z., & Cheng, K. S. 2014, *ApJ*, 785, 131
- Tendulkar, S. P., Yang, C., An, H., et al. 2014, *ApJ*, 791, 77
- Thorstensen, J. R. & Armstrong, E. 2005, *AJ*, 130, 759
- Turner, M. J. L. 2001, *A&A*, 365, L27
- van Haarlem, M. P., Wise, M. W., Gunst, A. W., et al. 2013, *A&A*
- Wang, Z., Archibald, A. M., Thorstensen, J. R., Kaspi, V. M., Lorimer, D. R., Stairs, I., Ransom, S. M. 2009, *ApJ*, 703, 2017
- White, N. E., & Swank, J. H. 1982, *ApJ*, 253, L61
- Wijnands, R., & van der Klis, M. 1998, *Nature*, 394, 344
- Woudt, P. A., Warner, B., Pretorius, M. L. 2004, *MNRAS*, 351, 1015
- Zampieri, L., Turolla, R., Zane, S., & Treves, A. 1995, *ApJ*, 439, 849x
- Zavlin, V. E., Pavlov, G. G., & Shibanov, Yu. A. 1996, *A&A*, 315, 141